ELSEVIER

Contents lists available at ScienceDirect

# Geochimica et Cosmochimica Acta

journal homepage: www.elsevier.com/locate/gca





# Source and fate of atmospheric iron supplied to the subarctic North Pacific traced by stable iron isotope ratios

Minako Kurisu<sup>a,\*</sup>, Kohei Sakata<sup>b</sup>, Jun Nishioka<sup>c</sup>, Hajime Obata<sup>d</sup>, Tim M. Conway<sup>e</sup>, Hannah R. Hunt<sup>e</sup>, Matthias Sieber<sup>e</sup>, Katsuhiko Suzuki<sup>a</sup>, Teruhiko Kashiwabara<sup>a</sup>, Sayuri Kubo<sup>f</sup>, Makoto Takada<sup>g</sup>, Yoshio Takahashi<sup>h</sup>

- <sup>a</sup> Submarine Resources Research Center, Research Institute for Marine Resources Utilization, Japan Agency for Marine-Earth Science and Technology, 2-15 Natsushima, Yokosuka, Kanagawa 237-0061, Japan
- <sup>b</sup> Earth System Division, National Institute for Environmental Studies, 16-2 Onogawa, Tsukuba, Ibaraki 305-8506, Japan
- c Pan-Okhotsk Research Center, Institute of Low Temperature Science, Hokkaido University, 19N, W8, Kita-ku, Sapporo, Hokkaido 060-0819, Japan
- <sup>d</sup> Atmosphere and Ocean Research Institute, The University of Tokyo, 5-1-5 Kashiwanoha, Kashiwa, Chiba 277-8564, Japan
- e College of Marine Science, University of South Florida, St. Petersburg, Fl. 33701, USA
- <sup>f</sup> Earth Surface System Research Center, Research Institute for Global Change, Japan Agency for Marine-Earth Science and Technology, 2-15 Natsushima, Yokosuka, Kanagawa 237-0061, Japan
- g Marine Works Japan Ltd., 3-54-1, Higashi, Oppama, Yokosuka, Kanagawa 237-0063, Japan
- h Department of Earth and Planetary Science, Graduate School of Science, The University of Tokyo, 7-3-1 Hongo, Bunkyo-ku, Tokyo 113-0033, Japan

#### ARTICLE INFO

Associate editor: Caroline P. Slomp

Keywords:
Iron stable isotope
Aerosol
Surface seawater
Iron speciation
GEOTRACES

#### ABSTRACT

The availability of dissolved iron (Fe) limits primary production over some regions of the surface ocean, especially in regions such as the subarctic North Pacific. In this work, we use Fe stable isotope ratios (8<sup>56</sup>Fe) in bulk and size-fractionated marine aerosol particles and dissolved Fe of surface seawater in the subarctic North Pacific on Japanese GEOTRACES cruise GP02 (Summer 2017) as a tracer to clarify the relative contribution of combustion and natural Fe in both marine aerosol particles and surface seawater. The bulk aerosols collected in the coastal regions of both East Asia and western North Pacific have total  $\delta^{56}$ Fe values that are as low as -0.5 ‰ when compared to crustal (+0.1 %), with both the water-soluble phase and the fine particles even more fractionated (as low as -1.9 and -2.8 %, respectively). The negative correlation between the aerosol  $\delta^{56}$ Fe signatures and the enrichment factors of Fe and other elements dominated by anthropogenic sources (e.g., lead and cadmium) in these coastal regions indicates the presence of Fe emitted from high-temperature combustion sources, such as coal combustion and metal smelting. In these regions, combustion Fe accounts for 4-13 and 13-45 % of the total and water-soluble aerosol Fe, respectively. The results demonstrate that soluble aerosol Fe sourced from combustion Fe can be equivalent to that sourced from natural dust Fe in these coastal regions. By contrast, the aerosol particles in pelagic regions were near crustal  $\delta^{56}$ Fe in all particle size fractions, indicating the dominance of natural Fe and little to no combustion Fe. The relationships among the fractional Fe solubility, major ion concentration, Fe species, and  $\delta^{56}$ Fe indicate that the presence of combustion Fe is the dominant reason for the solubility increase in the coastal regions and that the atmospheric processing of mineral dust during transport is more important in the pelagic regions. The dissolved Fe of the surface seawater at 10 m depth had a consistently higher  $\delta^{56}$ Fe by up to +1.5 % than that of the simultaneously collected water-soluble aerosol Fe. The pattern of the elevated  $\delta^{56}$ Fe in the surface seawater corresponds to decreasing Fe concentrations and can be approximated by Rayleigh fractionation; we attribute these elevated surface  $\delta^{56}$ Fe values to the effect of biological uptake. New Fe fluxes from both the atmosphere and deeper depths are limited at least in summer compared with the biological uptake in the open ocean of the subarctic North Pacific.

<sup>\*</sup> Corresponding author at: Atmosphere and Ocean Research Institute, The University of Tokyo, 5-1-5 Kashiwanoha, Kashiwa, Chiba 277-8564, Japan. E-mail address: minako-kurisu@g.ecc.u-tokyo.ac.jp (M. Kurisu).

#### 1. Introduction

The subarctic North Pacific is a high-nutrient, low-chlorophyll (HNLC) region, wherein primary production is constrained by bioavailable iron (Fe), leading to the underutilization of macronutrients in surface seawater (Martin and Fitzwater, 1988; Tsuda et al., 2003, 2007; Boyd et al., 2007). Thus, addition of dissolved Fe (dFe) to HNLC surface waters can stimulate the growth of microorganisms, which consequently influence overall nutrient utilization and ocean–atmosphere carbon dioxide (CO<sub>2</sub>) transfer, and act to influence the atmospheric CO<sub>2</sub> and the global climate (Falkowski et al., 1998; Ciais et al., 2014). The western subarctic North Pacific is considered as one of the largest CO<sub>2</sub> sinks due to biological activity in the oceans (Takahashi et al., 2002); hence, understanding how Fe is supplied to this region is especially important.

Away from continental margins, atmospheric aerosol particles are an important source of dFe in surface oceans (Jickells et al., 2005; Mahowald et al., 2005). There are several sources of Fe-bearing aerosol particles, including mineral dust (Duce et al., 1980; Uematsu et al., 1983, 1985), anthropogenic activities (Sedwick et al., 2007; Takahashi et al., 2013; Ito et al., 2019), biomass burning (Guieu et al., 2005; Ito, 2011; Perron et al., 2022; Hamilton et al., 2022), and volcanism (Uematsu et al., 2004; Hamme et al., 2010). Mineral dust and anthropogenic aerosols are thought to be the most important sources to the North Pacific, with the importance of mineral dust transport well established (e.g. Uematsu et al., 1983; Duce and Tindale, 1991; Measures et al., 2005). Asian dust is transported eastward from China and Mongolia. The maximum dust transport occurs in spring, that is, from February to June  $(\sim 7.8 \,\mu g \, m^{-3})$ , and are significantly lower in other seasons (i.e., July to January;  $\sim 1.2 \,\mu g \,m^{-3}$ ) in  $160^{\circ} E - 150^{\circ} W$  in the North Pacific (Uematsu et al., 1983; Parrington and Zoller, 1984). The strong spatial variability (deceasing from west to east) and the strong seasonal variability (highest in spring) in aerosol Fe fluxes have also been confirmed by the US CLIVAR and GEOTRACES cruises across the North Pacific (Buck et al., 2006, 2013; Marsay et al., 2022).

Anthropogenic aerosols are emitted by both non-combustion and combustion processes. Non-combustion emissions mainly include road dust and tire wear, whereas emissions from combustion processes mainly include fuel combustion, smelting, incineration, and engine combustion, among others (Seinfeld and Pandis, 2006). The particle sizes from combustion emission are typically finer than the mineral dust and non-combustion sources; therefore, combustion aerosol particles may be transported at longer distances (Willeke and Whitby, 1975). The combustion products of Fe are also highly soluble or easily become soluble by reaction with acids during transport (Schroth et al., 2009; Chen et al., 2012). Therefore, although combustion aerosol emission is an order of magnitude smaller than mineral dust emissions (Myriokefalitakis et al., 2018), the relative contribution of combustion Fe to the soluble phase in atmospheric aerosols is increasingly being considered important (Myriokefalitakis et al., 2018; Mahowald et al., 2018; Ito et al., 2021). The Asian dust transport to the North Pacific surface is likely to contain a mixture of natural and anthropogenic aerosol Fe components, with anthropogenic Fe being more soluble and relevant to surface water dFe inventories.

Iron may also reach the North Pacific surface from other sources. For example, elevated dFe of over 1 nmol kg $^{-1}$  is thought to be transported to the western subarctic North Pacific within the North Pacific Intermediate Water (NPIW; Nishioka and Obata, 2017; Nishioka et al., 2021) typically defined under the 26.6–27.5 $\sigma_{\theta}$  density range (Reid, 1965; Yasuda et al., 2001). The dFe sourced from rivers and resuspension of coastal sediments in the western part of the Sea of Okhotsk or Bering Sea is transported via intermediate waters, contributing to the formation of an Fe-rich NPIW, which then remarkably spreads all throughout the North Pacific (over 3000 km) at intermediate depths (Nishioka et al., 2007, 2011, 2014; Uchimoto et al., 2014; Nishioka and Obata, 2017; Wong et al., 2022). The dFe in NPIW at intermediate depths of

approximately 200–1500 m can mainly be brought to the surface by winter vertical mixing when the mixed layer depth is over 100 m, which causes seasonal phytoplankton blooms in the western subarctic North Pacific every year (Fujiki et al., 2022), although questions remain how important this source is to the mixed layer across the whole subarctic Pacific. In the eastern North Pacific, the dissolved and particulate Fe sourced from continental margins and via the Haida eddies is suggested to as a potentially important, yet spatially variable, Fe source to intermediate and surface waters (Johnson et al., 1997; Lam and Bishop, 2008; Xiu et al., 2011; Crusius et al., 2011).

Given the competing potential sediment and atmospheric Fe sources to the surface of the North Pacific, it is important to be able to spatially and temporally constrain their relative importance. Here, the stable isotope ratio of Fe ( $\delta^{56}$ Fe) may be a useful tool for distinguishing and tracing Fe sources both in the atmospheric aerosols and in the surface seawater itself (Dauphas et al., 2017). The use of  $\delta^{56}$ Fe measurements in seawater are well reviewed in Fitzsimmons and Conway (2023). Overall, the  $\delta^{56}$ Fe of dFe of seawater ranges from -4 to +2 % due to (i) the combination of mixing different external Fe sources, including atmospheric deposition (-4.1 to +0.3 %), Fe released from sediments (-3.5to -1.5 %), hydrothermal vents (-4 to +2 %), riverine input (-1.3 to +0.8 %), or due to (ii) isotope fractionation processes during internal ocean cycling, such as biological uptake, scavenging, regeneration, redox, and Fe complexation. A range of seawater studies have now been conducted to constrain the distribution of  $\delta^{56}$ Fe of dFe and the influence of different Fe sources in several ocean regimes across all ocean basins (e.g., Radic et al., 2011; Conway and John, 2014, 2015; Abadie et al., 2017; Sieber et al., 2021; Fitzsimmons and Conway, 2023). While only one study focused on the open North Pacific ocean (Conway and John, 2015), the works demonstrated that the influence of external sources (e. g., margin sediments) can clearly be seen as influencing  $\delta^{56}$ Fe of dFe, highlighting its utility in this region.

As regards aerosols, anthropogenic combustion aerosol particles can yield  $\delta^{56}$ Fe as low as -4.1 % (Mead et al., 2013; Kurisu et al., 2016a, 2016b, 2019), which is much lower than that of mineral dust aerosol particles (average: +0.1 %; Beard et al., 2003). Such low  $\delta^{56}$ Fe values are obtained due to the isotope fractionation during high-temperature evaporation and combustion processes (Kurisu et al., 2019). This large variability in the  $\delta^{56}$ Fe endmembers from distinct aerosol sources means that  $\delta^{56}$ Fe can be used to determine their relative contribution to a discrete aerosol sample. Several studies have indicated that isotopically light δ<sup>56</sup>Fe values in both total and water-soluble aerosols originated from combustion Fe, even in marine aerosols collected over both the North Atlantic and Pacific oceans (Conway et al., 2019; Kurisu et al., 2021). Discrete signatures for different aerosol Fe types have also been incorporated into the first attempts of modeling  $\delta^{56}$ Fe in oceans (König et al., 2022). However, the  $\delta^{56}$ Fe data in marine aerosols, especially over the open ocean, generally remain very limited, consequently restricting the utility of Fe stable isotope ratios as a tracer. The large contribution of either natural or combustion Fe derived from the atmosphere in surface seawater might be traced with  $\delta^{56} Fe$  in surface seawater. Pinedo-González et al. (2020) related the low  $\delta^{56}$ Fe values observed in the surface seawater in the North Pacific to anthropogenic aerosols. However, no data on the  $\delta^{56}\mbox{Fe}$  of the aerosol particles were obtained in the same area. Alternatively, if the  $\delta^{56}$ Fe signature of surface water is more strongly influenced by the biological uptake and recycling processes, the surface water  $\delta^{56}$ Fe may not reflect an anthropogenic input (e.g. König et al., 2022). Thus, concomitant seawater and aerosol  $\delta^{56}$ Fe is necessary to assess the applicability of Fe isotope ratios as a tracer of Fe in the surface ocean.

In the present study, we near-simultaneously collected aerosol particles and surface seawater as part of the Japanese GEOTRACES section GP02 in the subarctic North Pacific from June to August 2017, providing a direct comparison of the relevant  $\delta^{56} \text{Fe}$  values in aerosols and surface seawater from the same location in order to estimate the impact of combustion and natural Fe in marine aerosols and in the surface

seawater over the subarctic North Pacific. Fe species in the aerosols were also analyzed to help us better understand aerosol sources and controls on Fe solubility. We then use these results to investigate if aerosol  $\delta^{56}\text{Fe}$  is directly reflected in surface seawater or, if not, what factors determine the  $\delta^{56}\text{Fe}$  of the surface seawater. Overall, the near-simultaneous observation of the  $\delta^{56}\text{Fe}$  of aerosols and seawater in the open ocean enabled us to trace the atmospheric Fe upon deposition to the surface seawater. We show the contrasting influence of combustion Fe in aerosol particles from coastal and pelagic regions, and also the importance of phytoplankton uptake in controlling the  $\delta^{56}\text{Fe}$  of the surface seawater post-deposition.

#### 2. Methods

#### 2.1. Sampling

#### 2.1.1. Aerosols

The aerosol samples were collected during the R/V Hakuho-maru KH-17-3 Japanese GEOTRACES GP02 cruise from June 23 to August 6, 2017 across the subarctic North Pacific (samples A1 to A17; Fig. 1). We collected two types of aerosol samples: total suspended (i.e., bulk, not size fractionated) and six-size fractionated particles, in which natural and anthropogenic tend to be more concentrated in the coarse and small size fractions, respectively. The bulk was collected on a filter using a high-volume air sampler (KIMOTO, Model-120SL, Japan) at a flow rate of 1132 L min<sup>-1</sup>. The size-fractionated aerosol samples were collected using a Sierra-type cascade impactor (TE-235, Tisch Environmental Inc., USA) installed on another high-volume air sampler of the same type. The particles were separated into six stages (i.e., Stage 1, >7.2 μm; Stage 2,  $3.0-7.2 \mu m$ ; Stage 3,  $1.5-3.0 \mu m$ ; Stage 4,  $0.95-1.5 \mu m$ ; Stage 5,  $0.49-0.95 \,\mu\text{m}$ ; and backup filter (BF),  $<0.49 \,\mu\text{m}$ ) at a flow rate of 1132 L min<sup>-1</sup>. We defined the coarse and fine particles as stages 1–4 (coarser than 0.95  $\mu$ m) and 5-BF (finer than 0.95  $\mu$ m), respectively, to match GEOTRACES definitions. Using a wind sector controller, the air samplers were operated only when the relative wind direction was from  $-90^{\circ}$  to  $90^{\circ}$  of the bow, and the relative wind speed was higher than 1 m s<sup>-1</sup>. Each sampling period lasted for approximately 24h. Seventeen samples were collected, as shown in Table S1. The sampling points were categorized into four regions: East Asian coast, samples A1 to A3: pelagic region, samples A4 to A8 and A13 to A15; Alaskan coast, samples A9 to A12; and western North American coast, samples A16 and A17. After sampling, the filters were put into a polyethylene bag and stored in a

desiccator (RH <30 %). Sample treatment was performed in a clean bench under high-efficiency particulate air (HEPA)-filtered conditions.

Acid-washed polytetrafluoroethylene (PTFE) was used for both the TSP and size-fractionated aerosol sampling to increase the signal-to-filter background ratio (Sakata et al., 2018). Supplementary Materials present the detailed method for the filter preparation.

#### 2.1.2. Seawater

Seawater sampling was conducted during the same cruise (stations CL-1 to 21). The surface seawater samples at 10 m depth were collected at stations CL-1, 2, 5, 7, 9, 11, 14, 16, 17, and 20 (Fig. 1). Two lowresolution depth profiles of the  $\delta^{56}\mbox{Fe}$  of dFe in the western and eastern North Pacific (CL-2 and 16) were analyzed to further constrain the Fe cycle within the ocean and for inter-comparison purposes. At Station CL-2 (Ocean Station "K2," 47°N, 160°E) samples were collected at depths of chlorophyll a (Chl a) concentration maximum (16 m), dissolved oxygen (DO) concentration minimum (545 m), 1000 m, and 2000 m. At Station CL-16 (Ocean Station "PaPa," 50°N, 145°W), the samples were collected at Chl a maximum (25 m), 1000 m, DO minimum (1117 m), and 2000 m. The seawater sampling method was previously described (Nishioka and Obata, 2017; Wong et al., 2022). Briefly, the seawater samples were collected using acid-cleaned Teflon-coated 12 L Niskin-X bottles (General Oceanics, USA) mounted on a clean conductivity-temperature-depth carousel multiple sampler system (CTD-CMS, SBE-32, Seabird, USA) attached to the end of a Vectran armored cable. Sub-sampling from the Niskin-X sampler was performed in a clean space filtered with HEPA-filtered air on board. The samples were filtered using a polyethersulfone membrane filter (Acropak-200 filter; pore size: 0.2 µm; Pall Corp., USA). Subsequently, 10 L each of the filtered seawater sample was collected in a high-density polyethylene (HDPE) bottle (Nalgene, Round HDPE Carboy with handle, Thermo Fisher Scientific, USA). The bottles were cleaned prior to use by successively filling them with 5 % alkaline surfactant (Extran MA01, Merck, Germany) for 1 day, 4 mol L<sup>-1</sup> HCl (Electronics Industry grade, Fujifilm Wako Pure Chemical Corp., Japan) for 2 days, 0.1 mol L<sup>-1</sup> HCl (Tamapure AA-100, Tama Chemical Co., Ltd., Japan) for 2 days, and ultrapure water for 1 day. The seawater samples were acidified to pH  $\sim 2$ with HCl (Tamapure AA-10, Tama Chemical Co., Ltd., Japan) in a clean room onboard.

Supplementary Materials present the methods for analyzing parameters other than Fe, including Chl *a*, nutrients, and DO.

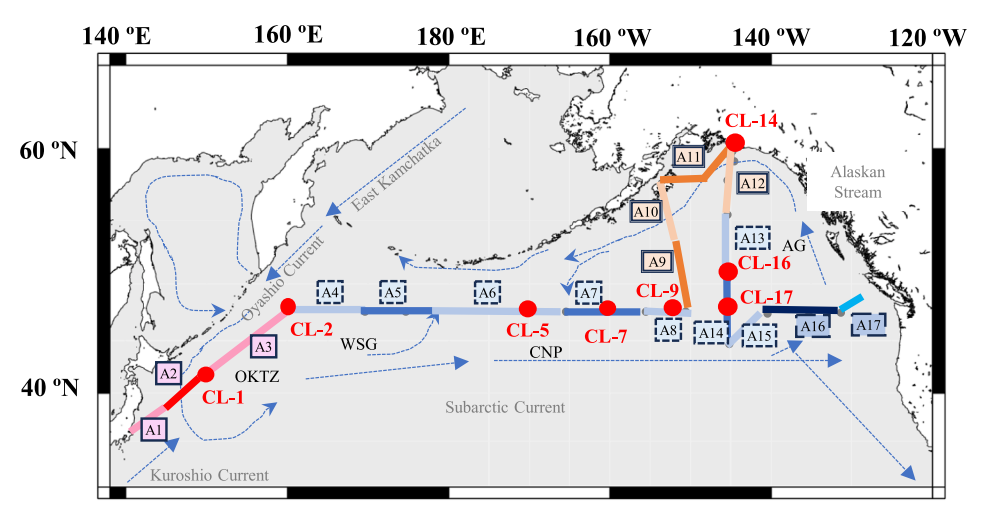


Fig. 1. Ship track of the KH-17-3 (Japanese GEOTRACES GP02) cruise. Different line colors indicate each aerosol sampling area (samples A1 to A17). The aerosol samples were categorized into four: East Asian coast (samples A1 to A3, pink); pelagic region (samples A4 to A8, and A13 to A15, light blue); Alaskan coast (samples A9 to A12, brown); and the western North American coast (samples A16 and A17, blue). The red circles are the seawater sampling sites. The stations were located in four surface ocean sections: the Oyashio-Kuroshio transition zone (OKTZ; Station CL-1); western subarctic gyre (WSG; Station CL-2); the Alaskan gyre (AG; stations CL-7, 9, 16, and 17); and central subarctic Pacific (CNP; Station CL-5). The dotted arrows indicate the surface currents.

#### 2.2. Sample processing of aerosol samples

# 2.2.1. Acid digestion of the aerosol particles for total elemental concentration analysis

Both bulk and size-fractionated aerosol samples were analyzed for Fe, aluminum (Al), vanadium (V), manganese (Mn), nickel (Ni, only bulk data were used for discussion), copper (Cu), zinc (Zn), cadmium (Cd), and lead (Pb) through inductively coupled plasma-quadrupole mass spectrometry (ICP-MS, NexION350s, Perkin Elmer, Inc., USA). Sample digestion was conducted with the same method as Kurisu et al. (2021). The aerosol samples collected on approximately 1/10–1/5 of the filter were digested with 2 mL of 15.2 mol L<sup>-1</sup> HNO<sub>3</sub>, 2 mL of 9.3 mol  $\rm L^{-1}$  HCl, and 1 mL of 22 mol  $\rm L^{-1}$  HF (Tamapure AA-100 grade, Tama Chemical Co., Ltd., Japan) at 150 °C for 1 day in an acid-washed 7 mL perfluoroalkoxy alkane (PFA) vial (Savillex, USA). After evaporation at 150 °C, the residue was digested with 2 mL of 15.2 mol L<sup>-1</sup> HNO<sub>3</sub> at 150 °C for 1 day and evaporated to dryness. An appropriate amount of 0.3 mol L<sup>-1</sup> HNO<sub>3</sub> was added to the sample for the ICP-MS measurement. All procedures were performed under HEPA-filtered conditions. The recovery was checked by analyzing CJ-2 (simulated Asian mineral dust, Nishikawa et al., 2000), Urban Aerosols (NIES CRM No. 28, Japan, Mori et al., 2008), and Arizona Test Dust (ATD, 0-3 µm, Powder Tech. Inc., USA, Table S2). The Fe contribution from a blank filter was 0.33  $\pm$ 0.12 (SD) ng cm $^{-2}$  filter for stages 1–5 and  $0.71 \pm 0.19$  ng cm $^{-2}$  filter for bulk and BF filters, respectively (for other elements, see Table S3). The blank concentration of each element was subtracted from the sample concentration. The Fe blanks, which corresponded to 31 and 153 pg m<sup>-3</sup> with an average sampling volume of 1400 m<sup>3</sup> corresponding to a sampling duration of 20h, were lower than those in previous studies using different filter types (Morton et al., 2013). The samples with a blank contribution higher than 20 % were not used for the isotopic and solubility analyses considering that the blank largely influenced the  $\delta^{56}$ Fe values and the fractional Fe solubility (the blank contribution is shown in our Mendeley dataset).

The trace metal concentrations of the bulk aerosol samples were almost consistent with the summation of each elemental concentration of the size-fractionated aerosol samples, ensuring that similar samples were collected during the bulk and size-fractionated aerosol sampling.

The enrichment factors (EF) of these elements were calculated as follows:

$$EF = (C_{\rm M}/C_{\rm Al})_{aerosol}/(C_{\rm M}/C_{\rm Al})_{crust} \tag{1}$$

where M is the target element, and  $(C_M/C_{Al})$  is the mass concentration ratio. Aluminum was used as the lithogenic tracer. The  $(C_M/C_{Al})_{crust}$  data were obtained based on the average upper continental crustal composition (Turekian and Wedepohl, 1961; Taylor, 1964; Hans Wedepohl, 1995; Taylor and McLennan, 1995; Rudnick and Gao, 2014). Considering the compositional variation, the element with an EF higher than 2 was considered to contain a large amount of anthropogenic components (Sakata et al., 2023).

# 2.2.2. Leaching of aerosol particles for the analysis of the water-soluble fraction of the trace elements

The water-soluble aerosol Fe concentrations were analyzed using a batch extraction method performed by soaking 1/10–1/20 of a sample filter in 5 mL of ultrapure water in an acid-washed LDPE vial with ultrasonic treatment for 30 min. After 24h, the samples were filtered with a 0.2  $\mu$ m hydrophilic PTFE filter (ADVANTEC, Japan). The extracted solution was then collected in an LDPE vial, acidified to 0.3 mol L<sup>1</sup> HNO<sub>3</sub>, and analyzed by sector-field ICP-MS (Element XR, Thermo Fisher Scientific, Germany) at Mutsu Institute for Oceanography, JAMSTEC. The fractional aerosol Fe solubility (Fe<sub>sol</sub>%) was calculated as follows:

$$Fe_{sol}\% = sol - Fe / total - Fe \times 100$$
 (2)

where the sol-Fe and total-Fe are mass concentrations of the water-

soluble and total (acid-digested) Fe, respectively. Table S3 presents the Fe contribution from a blank filter. For a comparison, a flow-through extraction was also conducted for the bulk aerosol samples, The details are described in Supplementary Materials.

The extracted solution was also used for the analysis of major ion concentrations with the method described in Supplementary Materials.

#### 2.3. X-ray absorption fine structure analysis of the aerosol samples

Iron speciation in the aerosol particles was performed through Fe Kedge X-ray absorption near-edge structure (XANES) analysis at the beamline BL-12C of the Photon Factory, High Energy Accelerator Research Organization (Ibaraki, Japan). The detailed optics of the beamline are described in the study of Nomura and Koyama (1996). Xray was monochromatized with a Si(111) double-crystal monochromator and focused with a bent cylindrical mirror. The higher order harmonics were removed using a Ni-coated double mirror. The X-ray energy was calibrated with a hematite pre-edge at 7.112 keV. The spectra were then recorded from 7.0 to 7.3 keV. The reference spectra were measured in a transmission mode using ionization chambers. Meanwhile, the sample measurements were conducted in fluorescence mode by placing the sample 45° from the incident beam. The Fe Kα line (6.41 keV) was detected with a seven-element silicon drift detector. Approximately 1/10 of the aerosol filter was used for the sample measurement. The aerosol particles on the filter were mounted on a Kapton tape to gather the particles at one point.

Subsequently, the linear combination fitting of the sample with the reference spectra was conducted using the REX2000 software (Rigaku Co., Ltd., Japan) with the same reference materials shown in Kurisu et al. (2021). The spectra were normalized at 7.250 keV. The fit quality was given by the goodness of the fit parameter (R value) defined as follows:

$$\Sigma R = \Sigma \{I_{obs}(E) - I_{cal}(E)\}^2 / \Sigma \{I_{obs}(E)\}^2, \tag{3}$$

where  $I_{obs}(E)$  and  $I_{cal}(E)$  are the experimental and calculated absorption coefficients, respectively at a given energy E. Samples with sufficient X-ray absorbance compared with that of a clean Kapton tape (approximately more than 5 times that of a new Kapton) were used for the discussion.

# 2.4. Iron isotope analysis

Iron isotope analysis was conducted using multi-collector ICP-MS (Neptune Plus, Thermo Fisher Scientific) either at the University of Tokyo (UT), JAMSTEC, or the University of South Florida (USF). The aerosols, some surface seawater, and one seawater profile (for intercomparison) were measured either at UT or JAMSTEC, while some surface seawater and two seawater profiles were measured at USF.

#### 2.4.1. Sample processing (UT/JAMSTEC)

The  $^{57}\text{Fe}^{-58}\text{Fe}$  double–spike (DS) technique was applied to realize a precise analysis (Rudge et al., 2009; Conway et al., 2013). Purified  $^{57}\text{Fe}$  and  $^{58}\text{Fe}$  metal powders were obtained from Isoflex (USA). Each metal was roughly weighed and digested in warm 6.6 mol L $^{-1}$  HNO<sub>3</sub> overnight. The two solutions were then mixed in an appropriate ratio and purified using 2.5 mL of anion exchange resin (AG-MP-1, 100–200 mesh, Bio-Rad laboratories Inc., USA) in a method scaled up from that described in the work of Kurisu et al. (2016b).

Aliquots of the digested or extracted aerosol samples were first spiked with the DS. The molar ratio of the DS to the sample was adjusted to 2:1 to minimize the measurement error (John, 2012). The solution was then evaporated to dryness and redissolved into 180  $\mu L$  of 15.3 mol  $L^{-1}$  HNO $_3$  (Tamapure AA-100, Tama Chemical Co., Ltd., Japan) and 20  $\mu L$  of 11.7 mol  $L^{-1}$  H $_2$ O $_2$  (Tamapure AA-100, Tama Chemical Co., Ltd., Japan) at 180  $^{\circ}$ C for 1 day. The solution was evaporated again and redissolved into 200  $\mu L$  of a 6 mol  $L^{-1}$  HCl + 0.3 mmol  $L^{-1}$  H $_2$ O $_2$  solution

for column purification by AG-MP-1 resin, as previously described (Kurisu et al., 2021). Briefly, the sample dissolved in a 6 mol  $L^{-1}$  HCl + 0.3 mmol  $L^{-1}$  H<sub>2</sub>O<sub>2</sub> solution was added into a prewashed and conditioned microcolumn filled with approximately 20  $\mu L$  of the resin. Subsequently, a 6 mol  $L^{-1}$  HCl + 0.3 mmol  $L^{-1}$  H<sub>2</sub>O<sub>2</sub> solution was added to remove the interfering elements. Purified Fe was collected into a PFA vial by adding a 1 mol  $L^{-1}$  HCl + 0.3 mmol  $L^{-1}$  H<sub>2</sub>O<sub>2</sub> solution. The purified solution was evaporated and redissolved into 180  $\mu L$  of 15.3 mol  $L^{-1}$  HNO<sub>3</sub> and 20  $\mu L$  of 11.7 mol  $L^{-1}$  H<sub>2</sub>O<sub>2</sub> at 180 °C for 1 day, and then evaporated again. The samples were redissolved into 0.3 mol  $L^{-1}$  HNO<sub>3</sub> for the successive isotope analysis. The recovery rate was 96  $\pm$  1 % (2 SD, n = 3).

Seawater samples were processed using the above mentioned method, but with the initial extraction and purification steps developed based on the work of Conway et al. (2013). Here, 2 or 4 L samples were used for shallow depths of less than 50 m and 1 L at depths deeper than 50 m. First, the seawater samples were spiked with the DS to achieve a DS-sample Fe molar ratio of approximately 2:1. Then,  $10 \mu mol L^{-1} H_2 O_2$ was added to ensure that all the Fe valence was Fe(III). After 24 h, 2.5 mL of pre-washed chelate resin (Nobias PA-1 chelating resin, Hitachi High Tech., Japan) was added to extract the trace metals from the seawater (Sohrin et al., 2008). After the addition of resin, the samples were shaken with a shaker (100–120 shakes min<sup>-1</sup>) for approximately 1 day. The resin was filtered with a pre-washed 0.4 µm polycarbonate filter (Advantec, Japan) attached to a 47 mm single-stage PTFE filter assembly (Savillex, USA). The separated resin that adsorbed trace metals in the sample was rinsed with ultrapure water to remove residual major salts. The trace metals were then eluted by adding 30 mL of 3 mol  $L^{-1}$ HNO<sub>3</sub> to the resin. The solution was collected in a PFA vial and evaporated to near dryness at 180  $^{\circ}\text{C}.$  The residue was redissolved into 180  $\mu L$  of 15.3 mol  $L^{-1}$  HNO3 and 20  $\mu L$  of 11.7 mol  $L^{-1}$   $H_2O_2$  at 180  $^{\circ}C$  for more than 2 h and evaporated again. It was then redissolved into 200  $\mu L$ of a 6 mol  $L^{-1}$  HCl + 0.3 mmol  $L^{-1}$  H<sub>2</sub>O<sub>2</sub> solution for the subsequent anion exchange column separation. The procedural blanks of the chelate resin extraction and anion exchange processes were 0.33  $\pm$  0.31 ng (SD, n=4) and 0.25  $\pm$  0.18 ng (n = 7), respectively, which together corresponded to  $\sim\!0.005$  nmol  $kg^{-1}$  in a 2 L seawater sample.

# 2.4.2. Fe isotope analysis (UT/JAMSTEC)

Considering the extremely low amount of Fe, a desolvating nebulizer system (Aridus II, CETAC Tec., USA) was used for the sample introduction. A PFA nebulizer with a flow rate of  $100~\mu L~min^{-1}$  was employed. A nickel jet sampling cone and a nickel X skimmer cone (Thermo Fisher Scientific, Germany) were adopted to obtain a high sensitivity. The high-resolution mode was adopted to resolve the argide interference.

The stable isotope ratio of Fe is expressed as  $\delta^{56}\mbox{Fe}$  as the following:

$$\delta^{56} \text{Fe} = \left( \frac{\left( {}^{56} \text{Fe} / {}^{54} \text{Fe} \right)_{\text{sample}}}{\left( {}^{56} \text{Fe} / {}^{54} \text{Fe} \right)_{\text{standard}}} - 1 \right) \times 1000 \, (\%) \tag{4}$$

where IRMM-014 from Institute for Reference Material and Measurements was used as the standard material.

The isotopic signals of  $^{52}\text{Cr}$ ,  $^{54}\text{Fe}$ ,  $^{56}\text{Fe}$ ,  $^{57}\text{Fe}$ ,  $^{58}\text{Fe}$ , and  $^{60}\text{Ni}$  were monitored.  $^{52}\text{Cr}$  and  $^{60}\text{Ni}$  were used to correct the isobaric interferences on  $^{54}\text{Cr}$  and  $^{58}\text{Ni}$ , respectively. The  $^{54}\text{Cr}$  and  $^{58}\text{Ni}$  interferences with  $^{54}\text{Fe}$  and  $^{58}\text{Fe}$  were less than 0.1 and 0.03 mol %, respectively, and did not cause any bias. Each sample was measured for 30 cycles of 4.2 s each. The  $8^{56}\text{Fe}$  calculation was conducted with the assumption that the instrumental and natural mass-dependent fractionation follows an exponential law according to Siebert et al. (2001). The Fe concentration of the seawater was analyzed by isotope dilution.

The isotopic composition of the DS solution was calibrated by measuring the pure IRMM, the DS, and DS—IRMM mixtures at various ratios. Following the DS calibration, the DS—IRMM mixtures at different

ratios were measured on each measurement day (Fig. S1a). The DS calibration yielded consistent  $\delta^{56} \text{Fe}$  for all mixtures, except for samples with the DS–IRMM ratios of 10:1 and 1:10. Therefore, although we set the DS–sample ratios to 2:1 to obtain a smaller error, the measured samples with ratios ranging from 5:1 to 1:5 were judged to be accurate. We checked the sensitivity by measuring different Fe concentrations of the IRMM (Fig. S1b). The typical signal intensity of  $^{56} \text{Fe}$  was 0.15–0.25 V per 1 ng g $^{-1}$ . The samples with concentrations higher than 25 ng mL $^{-1}$  (~4 V) could be measured with less error. If the sample Fe amount was sufficient, Fe concentration in the measurement solution was adjusted to 100 ng mL $^{-1}$ .

We checked the accuracy and the reproducibility of the measurement with Fe solution (iron standard solution Fe 1000, Fujifilm Wako Pure Chemical Corp., Japan) as a working standard on each measurement day. The  $\delta^{56} Fe$  values were almost identical (on average  $\delta^{56} Fe = +0.32 \pm 0.07$ % (2 SD), 32 runs of 30 cycles each) and consistent with those measured using the standard bracketing method in our previous studies ( $\delta^{56} Fe = +0.29 \pm 0.07$ %, 14 runs of 60 cycles each, Kurisu et al., 2019).

#### 2.4.3. Sample processing and Fe isotope analysis (USF)

The surface seawater and a selection of deep seawater samples were measured at USF by Kurisu in 2018 or Hunt in 2022-2023 (as part of the GP02 seawater Fe isotope section). A subset of the seawater samples (4 L for the surface samples and 1-2 L from two profiles at CL-2 and 16) was collected from the same Niskin bottles in an identical manner into lowdensity polyethylene bottles which had been acid cleaned by immersion in 1 mol L<sup>-1</sup> HCl for a week and thoroughly rinsed with ultrapure water, following the work of Conway et al. (2013). They were independently processed and analyzed for the Fe concentration and  $\delta^{56}$ Fe at the Tampa Bay Plasma Facility USF College of Marine Science, using DS methods previously described at length (full details of the method, analytical blanks, precision, and accuracy can be found in Sieber et al., 2021; Hunt et al., 2022). The precision of the  $\delta^{56}$ Fe data from this method was assumed as 0.05 ‰ based on the repeated analysis of the NIST 3126a iron standard solution ( $+0.36 \pm 0.05$  %; 2 SD, n = 524; runs = 37; Hunt et al., 2022). The precision and the accuracy of this method for the concentrations and the  $\delta^{56}$ Fe were also previously demonstrated (Conway et al., 2016; Sieber et al., 2021).

### 2.4.4. Inter-comparison between laboratories and overall precision

GP02 CL-2 and CL-16 samples analyzed at either UT, JAMSTEC, or USF (full procedural replicates) showed an excellent agreement in terms of Fe concentration and the  $\delta^{56}$ Fe (within uncertainty) between the samples, indicating the data accuracy for all laboratories (Table S4).

Most of the samples were measured only once due to the limited sample amounts. Thus, the adopted error was the 2 SE of each 30-cycle measurement or the 2 SD of the long-term working standard (i.e. 0.07 % for UT/JAMSTEC and 0.05 % for USF), whichever was larger, following Sieber et al. (2021). When the samples were measured more than once, including data from all laboratories, the weighted average and error were calculated as follows, with the calculated error used if > 0.07 %:

Weighted average = 
$$\frac{\sum (x_i/SE^2)}{\sum (1/SE^2)}$$
 (5)

Weighted SE = 
$$\sqrt{\frac{1}{\sum (1/SE)^2}}$$
 (6)

where  $x_i$  is the average  $\delta^{56}\text{Fe}$  of each 30-cycle measurment.

# 3. Results

### 3.1. Air mass sources

The backward trajectory analysis (NOAA HYSPLIT trajectory model;

run time: 168h; height: 500 m; Stein et al., 2015) was conducted for each sampling period (Figs. 2 and S2). The air masses were mainly from the west due to the westerlies. The air masses of the samples collected in the East Asian coast (samples A1-A3) mainly passed over the land area of Japan (Fig. 2a). In the pelagic region (samples A4-A8 and A13-A15), most samples contained maritime air masses from the west over the North Pacific and some samples (e.g., A4 and A5) got northern or northwestern air masses passing over eastern Siberia (Fig. 2b). Samples collected in the Alaskan coastal regions (A9-A12) often passed over the Alaskan mainland (Fig. 2c). In the western North American coast, air masses also contained maritime air masses, but they passed close to the land area of western North America (Fig. 2d).

#### 3.2. Trace element concentrations in aerosol particles

The total Fe concentrations in the bulk aerosol particles varied from 0.3 to  $62.4~\rm ng~m^{-3}$  (Fig. 3a). The highest concentrations were observed in the coastal region of East Asia (Sample A1). In contrast, the concentrations in the other regions were one to two orders of magnitude lower than those in the coastal region of East Asia. The concentrations of other elements and major ions, including Al, Mn, Cu, Zn, Cd, Pb, sulfate, and oxalate, showed similar spatial trends to Fe (Fig. S3). The V and Ni concentrations, often used as a tracer of oil combustion (Nriagu and Pacyna, 1988), showed different spatial trends; the concentrations were similar in the coastal regions and the other regions.

The EFs of Fe (average:  $1.29\pm0.41$ , SD) and Mn (average:  $1.67\pm0.82$ , SD) in the bulk were close to one in all regions (Figs. 3b and S4). By contrast, the EFs of V, Ni, Cu, Zn, Cd, and Pb, which are commonly found in anthropogenic aerosol particles, were higher than 10 (Fig. S4). The EFs of Zn, Cd, and Pb near the coastal regions of East Asia and western North America (samples A1-A3, A16, and A17) were higher than in the other regions, while those of V and Ni were highest in samples A6 and A7 in the pelagic region.

The size distribution of the trace element concentrations were averaged in each region (Figs. 4a and S5). Iron, Al, and Mn were more abundant in the coarse particles for most samples, which is a typical trend for crustal abundant elements (Willeke and Whitby, 1975). For instance, coarse particles accounted for 76  $\pm$  24 % (SD) of the Fe. Particularly high concentrations in the coarse particles were observed in the coastal region of East Asia. The concentrations of V, Cu, Zn, Cd, and Pb were higher in the fine particles than in the coarse ones, especially when the bulk concentrations were high as in samples A1 and A2.

The size-fractionated EF values were more elevated in the fine particles than in the coarse particles for all the measured elements (Figs. 4b and S6). Although the EFs of Fe and Mn in the bulk aerosols were close to

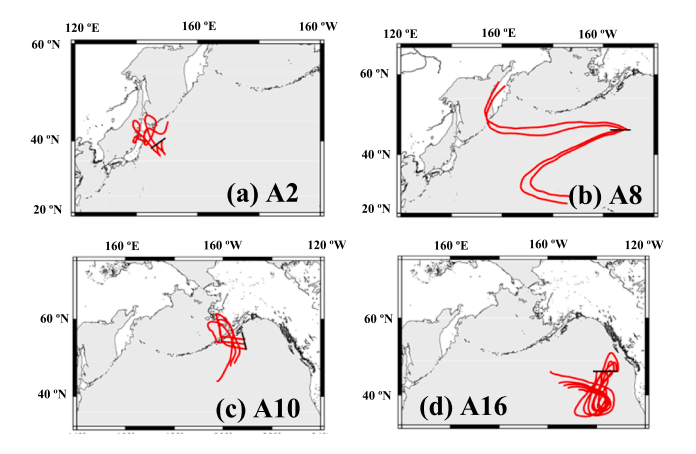


**Fig. 2.** Results of 168-hour air mass backward trajectory analysis of some aerosol samples along the ship track. Trajectory height was 500 m and the calculation was conducted every 6 h. Black line indicates the ship track. The trajectories of the other samples are shown in Fig. S2.

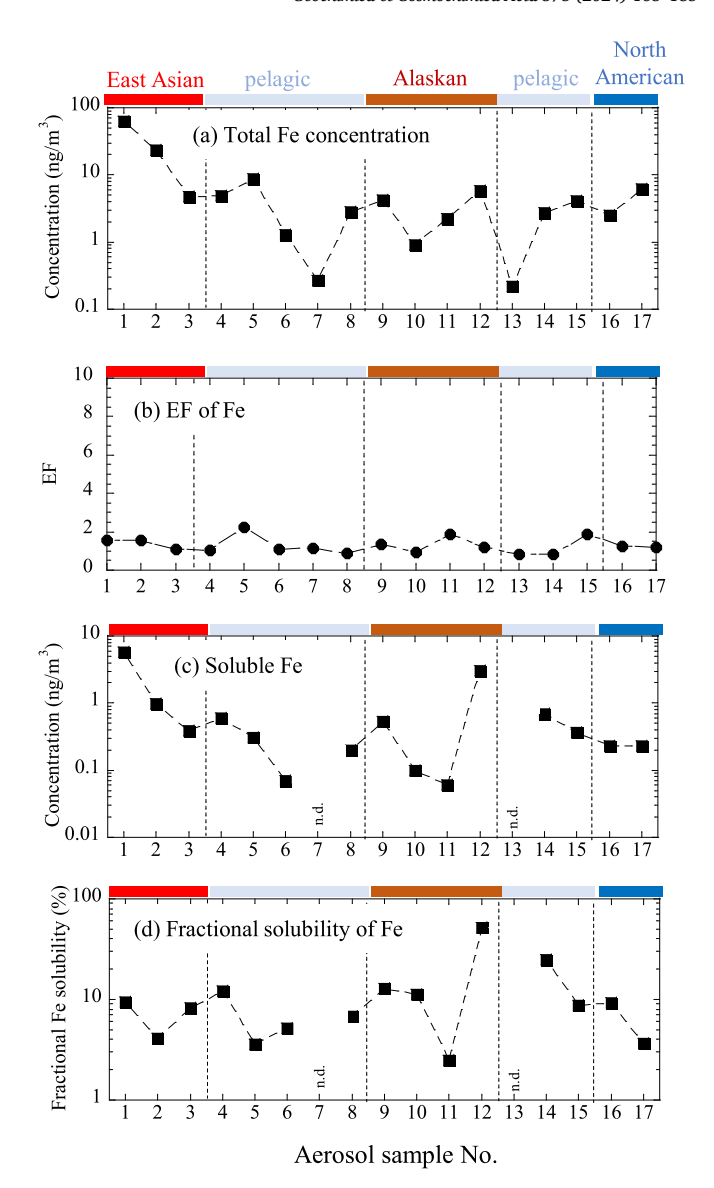


**Fig. 3.** (a) Atmospheric concentrations of the total Fe, (b) EF of Fe, (c) water-soluble Fe concentration, and (d) fractional Fe solubility for the bulk samples. Each color on the top of the graph means a different categorization: red: coastal region of East Asia; light blue: pelagic region; brown: Alaskan coastal region; and blue: coastal region of western North America. n.d.: not determined because the blank Fe contribution to the total Fe was high.

1, fine particles showed higher EFs than the bulk. The higher EF values in the fine particles were observed in all regions, particularly in the coastal region of East Asia.

# 3.3. Water-soluble Fe concentration and fractional solubility of Fe

The water-soluble Fe concentrations in the bulk aerosol particles obtained by batch extraction ranged from 0.05 to 5.8 ng m $^{-3}$ , with the highest concentration observed at Sample A1 near the Japanese coast (Fig. 3c). The spatial trend of the water-soluble Fe concentration was similar to that of the total Fe (Fig. 3a and c). The Fe $_{sol}\%$  ranged from 2.5 to 52 % (average: 11.6  $\pm$  12.4 %, SD, Fig. 3d). A particularly high Fe $_{sol}\%$  was found in samples A12 (52 %, near the Alaskan coast) and A14 (25 %, in the pelagic region).

The water-soluble Fe concentrations of the size-fractionated aerosol particles were only available for some of the samples, that tended to be higher in fine size fractions than in coarse ones (Fig. 4c), despite the total

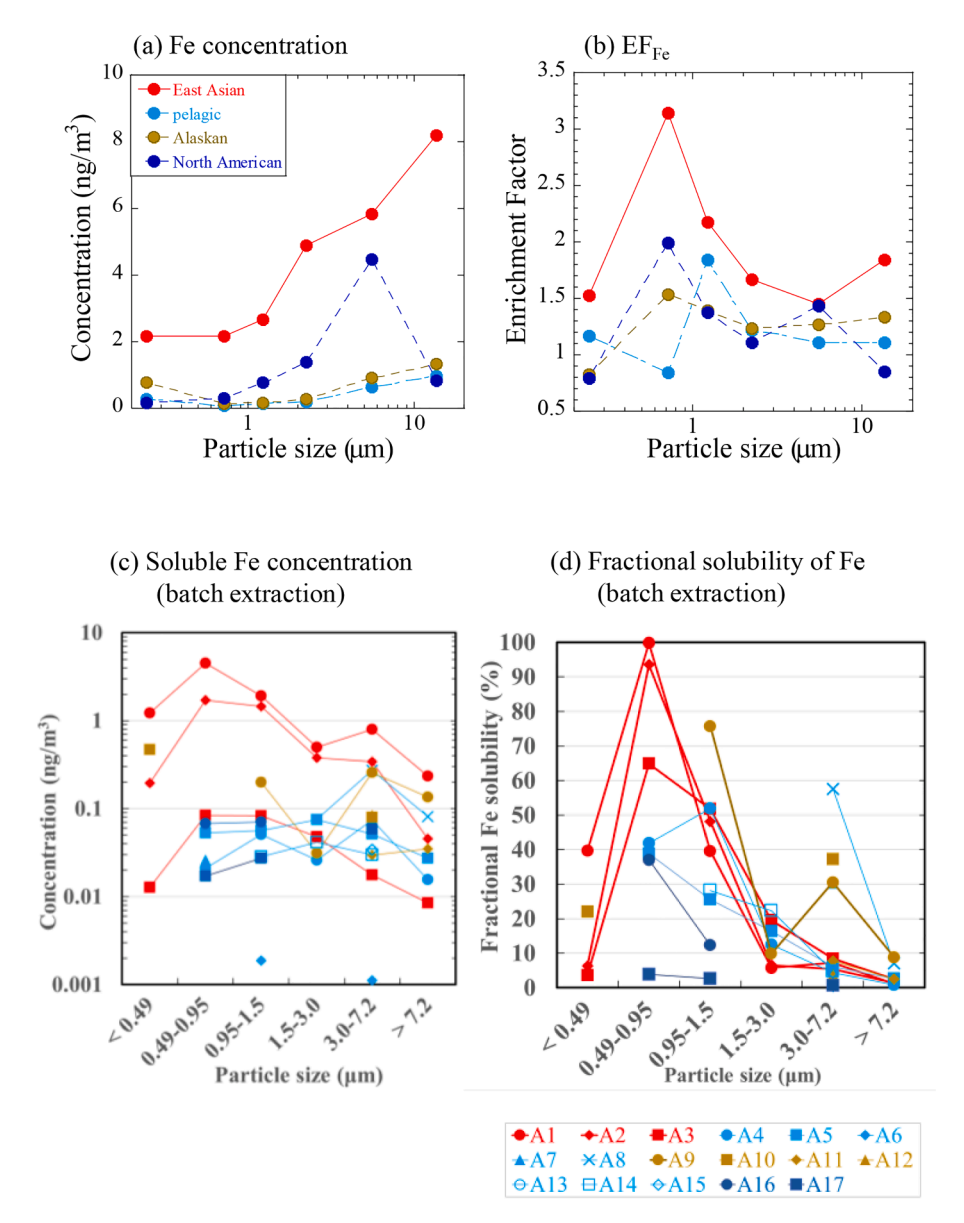


**Fig. 4.** Average size distribution of (a) the Fe concentration and (b) enrichment factors in each region. Size distribution of (c) the water-soluble Fe concentration and (d) the fractional Fe solubility.

Fe was rich in coarse size fractions. The Fe $_{sol}$ % was higher in the fine particles (on average 41 %) than in the coarse particles (on average 17 %, Fig. 4d). Particularly high solubilities above 60 % were observed in the 0.49–0.95  $\mu$ m size fraction (Stage 5) of samples A1 to A3 in the coastal region of East Asia.

The result of the flow-through extraction of the bulk aerosol particles is shown in the Fig. S7, where the solubility ranged from 2.1 to 17 % (average: 5.9  $\pm$  5.0 %) which was lower than the batch extraction (average: 11.6  $\pm$  12.4 %, SD, Fig. 3d). This is reasonable considering that the batch extraction can contact with aerosol particles for a longer time to gradually solubilize relatively less reactive Fe particles (Wu et al., 2007; Li et al., 2023).

#### 3.4. Iron speciation in the size-fractionated aerosol particles

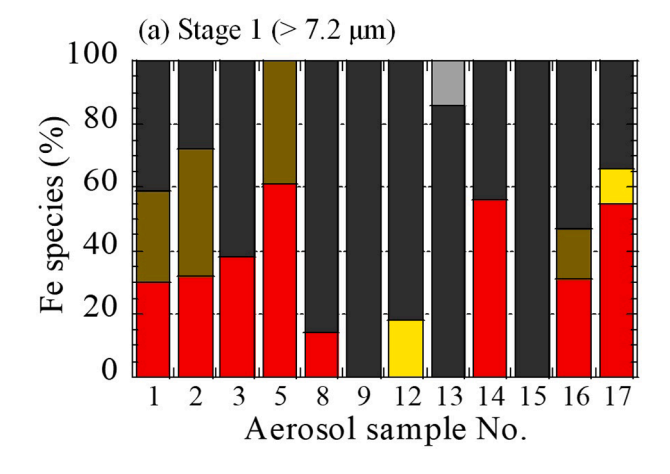
The linear combination fitting of the XANES spectra of the size-fractionated aerosol particles showed that the major Fe species were aluminosilicate minerals (such as illite, hornblende, and chlorite), ferrihydrite, Fe(III) sulfate, Fe(III) oxalate, and Fe(III) citrate (Figs. 5 and S8). Aluminosilicate minerals are commonly found in surface soils and

mineral dust in Asia or North America (Schroth et al., 2009; Takahashi et al., 2011, 2013; Ito and Wagai, 2017; Pattammattel et al., 2021) and more abundant in coarse particles than in fine ones. Chlorite, which has a characteristic peak shape around 7.12 keV (Fig. S8a), was found in all size fractions of Sample A12 near the Alaskan coast, but was absent in most of the other samples.

Ferrihydrite was observed in all size fractions in most samples (Figs. 5 and S8c-f). Fe(III) sulfate, Fe(III) oxalate, and Fe(III) citrate (and other analogous chelating ligands other than oxalate), which are highly soluble, were detected in particles finer than 1.5  $\mu$ m only. Iron (III) oxalate was only observed in samples A1 and A2 (near the Japanese coast). Iron (III) citrate was found in Sample A3. Iron (III) sulfate was found in the fine particles of samples A5, A12, A16, and A17.

# 3.5. Iron isotope ratios of aerosol particles

The  $\delta^{56}$ Fe of the total (acid-digested) fraction in the bulk ranged from -0.5 to +0.4 % (Fig. 6a and b, Table S5). The  $\delta^{56}$ Fe values were lowest in the coastal region of East Asia ( $-0.40 \pm 0.07$  % and  $-0.47 \pm 0.07$  % for samples A1 and A2, respectively). The  $\delta^{56}$ Fe of the other samples



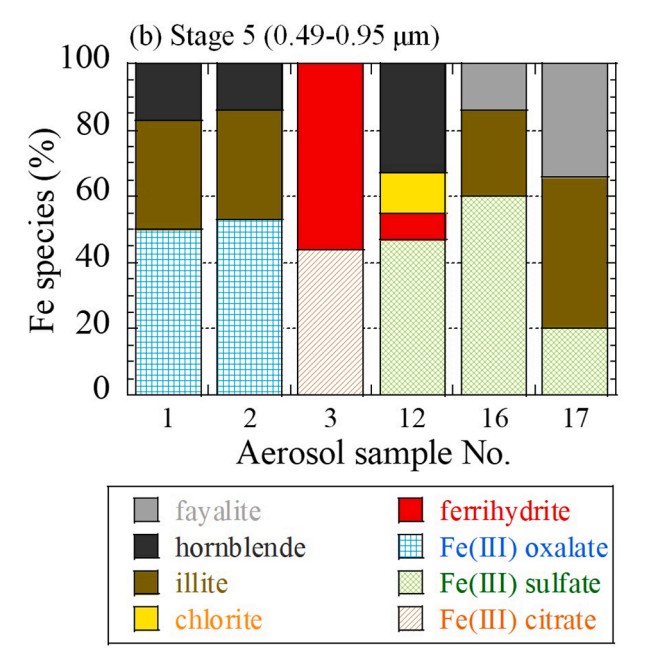


Fig. 5. Fe species of (e) stages 1 ( $>7.2~\mu m$ ) and (f) 5 ( $0.49-0.95~\mu m$ ). Species with filled colors indicate aluminosilicate or Fe oxide minerals. Shaded colors depict easily soluble species.

were within the typical  $\delta^{56}\text{Fe}$  range of mineral dust (-0.1 to +0.2 %), except for Sample A6 ( $+0.45\pm0.15$  %) from the pelagic western subarctic region.

The size-fractionated aerosol particles showed a larger  $\delta^{56}$ Fe range (-2.8 to +0.5 %, Fig. 6c-f). Note that the  $\delta^{56}$ Fe of the bulk (all the size fractions) aerosol particles was almost identical to that calculated from the concentration-weighted mean of  $\delta^{56}\text{Fe}$  of the size-fractionated aerosol samples, confirming consistent analysis results (Table S5). The  $\delta^{56}$ Fe values (down to  $-2.82 \pm 0.07$  %) were particularly low in the coastal regions of East Asia, with the lowest values observed in the  $0.49-0.95 \mu m$  (Stage 5) size fraction (Fig. 6c). Low  $\delta^{56}$ Fe values were also found in the fine particles in Sample A5 ( $-0.16 \pm 0.07$  % in the  $0.49-0.95 \mu m$  fraction) in the pelagic region and samples A16 and A17 (as low as -1.35 %) in the coastal region of western North America, although the bulk particles from the same locations having  $\delta^{56}$ Fe values close to the average mineral dust ( $+0.24 \pm 0.07$  ‰,  $-0.13 \pm 0.07$  ‰, and  $-0.03 \pm 0.07$  % at samples A5, A16, and A17, respectively) due to the relatively higher  $\delta^{56} Fe$  in the fine particles compared with those in samples A1 to A3. Conversely, the  $\delta^{56}$ Fe values of the particles coarser than 1.5 µm (stages 1-3) in the same samples (A1-A3, A5, A16, and A17, average:  $+0.02\pm0.13$  %, SD) were close to average mineral dust

composition.

The  $\delta^{56}$ Fe values in the Alaskan coastal and pelagic regions were mostly close to the average mineral dust in all size fractions, without size dependence. Samples A5 and A6 showed higher  $\delta^{56}$ Fe compared to the crustal average in the coarse size fraction (+0.35 and +0.48 % in >7.2  $\mu$ m size fraction, respectively), which was also observed in the bulk at these locations.

The  $\delta^{56}$ Fe of the water-soluble Fe of the bulk ranged from -1.87 to +0.28 ‰ (Fig. 6a). The lowest values were found in samples A1, A2, A16, and A17 in the coastal regions of East Asia and western North America. Overall, the water-soluble fractions showed similar or lower  $\delta^{56}$ Fe values than the total. The largest difference was observed in samples A1 and A2, for which the  $\delta^{56}$ Fe of the total fractions was also lower than those in the other samples.

#### 3.6. Dissolved seawater Fe concentrations and Fe isotope ratio

The surface seawater at 10 m depth in the coastal region of East Asia (CL-1 and 2) showed slightly high dFe concentrations of 0.09 and 0.08 nmol kg<sup>-1</sup>, respectively), and decreased toward the pelagic region (down to 0.02 nmol kg<sup>-1</sup>; the concentration data on these samples have already been reported in Nishioka et al., 2020; 2021; Fig. 7a). Our measured dFe concentrations of 0.02-0.03 nmol kg<sup>-1</sup> at the surface of CL-16, located at Ocean Station PaPa, were consistent with those in the previous measurements from that location over several decades (Martin et al., 1989; Nishioka et al., 2001; Schallenberg et al., 2015). Our measurements of the open-ocean surface values that were as low as 0.02 nmol kg<sup>-1</sup> in multiple replicates from 10 m at Station 16, which was in agreement with Nishioka et al. (2020), also confirmed that the samples were not contaminated during sampling or analysis (Table S4). Station CL-14, very close to the Alaskan coast showed the highest concentration of 0.34 nmol kg<sup>-1</sup>. The surface seawater, except in stations CL-1 and 14, can be assumed to be Fe-limited based on the ratio of dFe and nitrate  $\pm$ nitrite concentrations (Fig. S9, Supplementary Materials).

The  $\delta^{56} Fe$  of dFe in the surface seawater ( $\delta^{56} Fe_{dFe-surface}$ ) varied from -0.08% to +0.85% across the section (Fig. 7b), which were within the range reported in previous studies in the eastern North Pacific (0 to +1%; Conway and John, 2015; Fitzsimmons and Conway, 2023). At stations CL-1 ( $-0.11\pm0.07$ %), CL-2 ( $-0.08\pm0.07$ %), and CL-14 ( $+0.02\pm0.07$ %), where the dFe concentrations were higher than the other sites, the  $\delta^{56} Fe_{dFe-surface}$  values were close to the crustal average, and lower than those at the other sites. By contrast, the pelagic regions, where the dFe concentrations were relatively low, exhibited high  $\delta^{56} Fe_{dFe-surface}$  values (+0.45 to +0.84%).

Depth profiles of the dFe concentrations and the  $\delta^{56}$ Fe of the dFe ( $\delta^{56}$ Fe<sub>dFe</sub>) at stations CL-2 (Ocean Station K2, 47°N, 160°E) and CL-16 (Ocean Station PaPa, 50°N, 145°W) were also analyzed (Fig. 8). The mixed layer depth was approximately 10 m based on the temperature and salinity depth profiles (Fig. S10a and b). The dFe concentrations for both locations were very low (i.e., less than 0.1 nmol kg $^{-1}$ ) at the surface and became higher than 0.5 nmol kg $^{-1}$  below the intermediate depth, similar to previous studies (Martin et al., 1989; Nishioka et al., 2001, 2007; Schallenberg et al., 2015; Nishioka and Obata, 2017). Overall, the dFe concentrations were higher at Station CL-2 than in Station CL-16 by 0.05 nmol kg $^{-1}$  at the surface and by up to 0.8 nmol kg $^{-1}$  in the intermediate NPIW range (approximately 200–1000 m, 26.6–27.5  $\sigma_{\theta}$ ).

The  $\delta^{56}$ Fe<sub>dFe</sub> (10–2000 m depth) at CL-2 and 16 ranged from -1.36 to -0.08 % and -0.79 to +0.87 %, respectively (Fig. 8b). The highest  $\delta^{56}$ Fe<sub>dFe</sub> values were observed at the surface (10 m) for both locations. Below the surface, the  $\delta^{56}$ Fe<sub>dFe</sub> was much lower at the Chl a maximum at Station CL-2 (16 m,  $-1.01 \pm 0.07$  %) than at the surface (10 m,  $-0.08 \pm 0.07$  %). In contrast, Station CL-16 had similar  $\delta^{56}$ Fe<sub>dFe</sub> at both depths ( $+0.84 \pm 0.07$  % and  $+0.87 \pm 0.07$  % at 10 and 25 m, respectively), where a clear Chl a maximum was not observed (Fig. S10c). The lowest values were observed around the intermediate layers (200–1000 m), with the  $\delta^{56}$ Fe<sub>dFe</sub> at Station CL-2 ( $-1.37 \pm 0.07$  %) lower than at Station

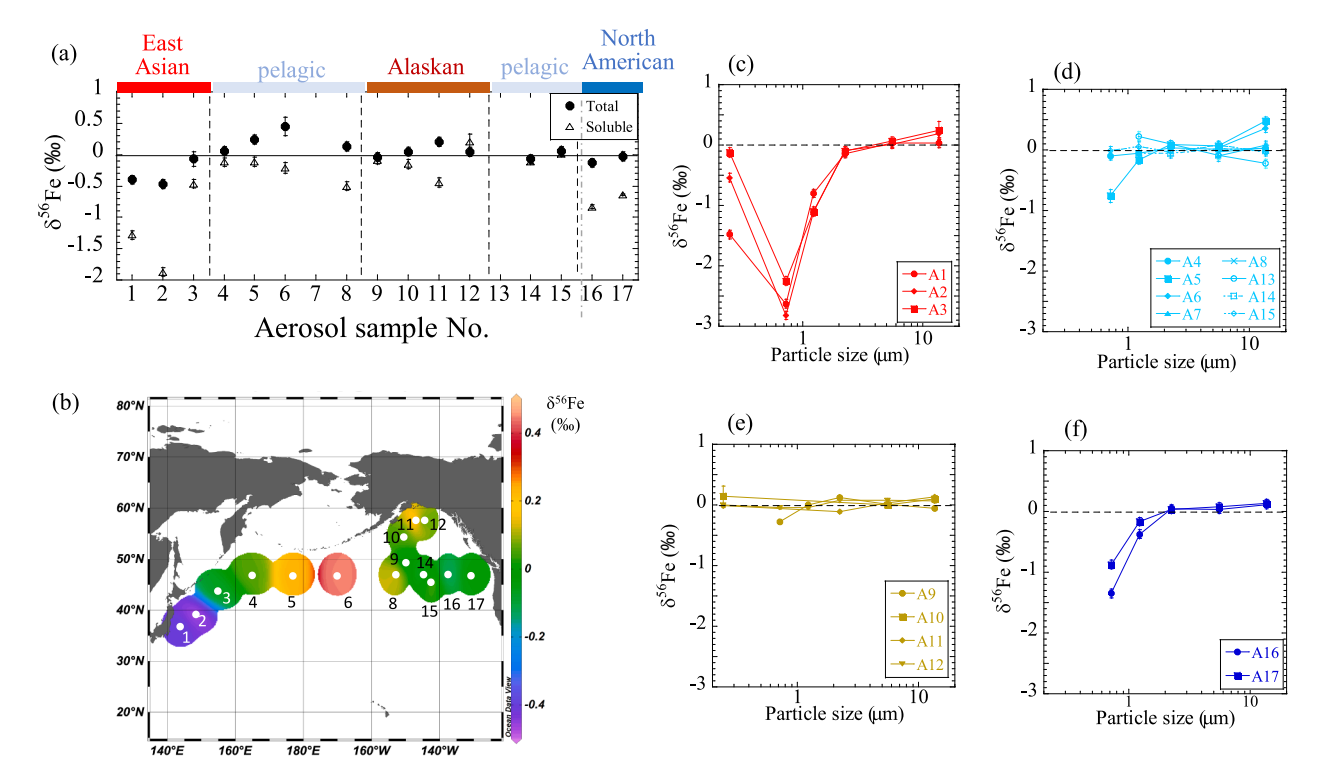


**Fig. 6.** (a) Iron isotope ratios of the total and water-soluble Fe in the bulk aerosol particles. Each color on the top of the graph means a different categorization: red: coastal region of East Asia; light blue: pelagic region; brown: Alaskan coastal region; and blue: coastal region of western North America. (b) Distribution of the δ<sup>56</sup>Fe of the total Fe. Size distribution of the δ<sup>56</sup>Fe of the aerosol particles in (c) coastal region of the East Asia, (d) pelagic region, (e) Alaskan coastal region, and (f) coastal region of western North America.

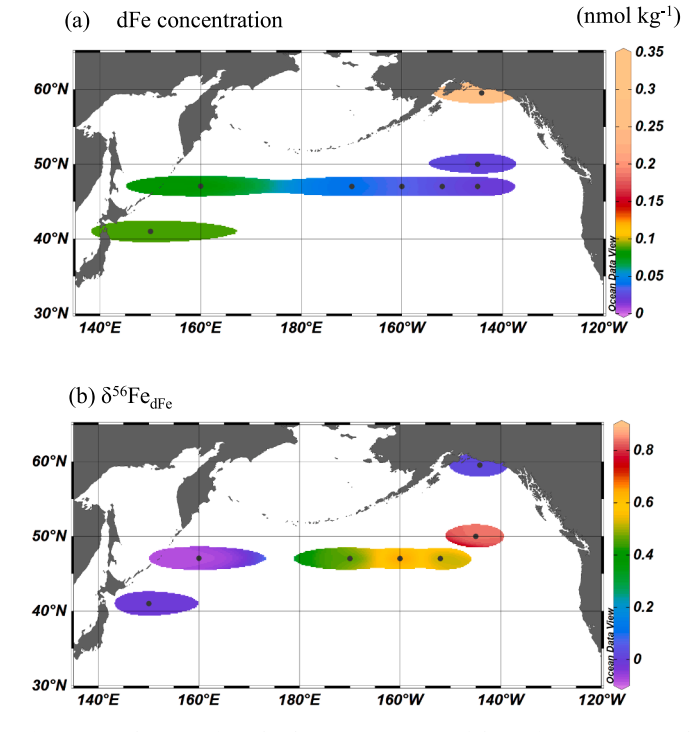


Fig. 7. Distributions of (a) the dFe concentrations of the surface seawater, and (b)  $\delta^{56}$ Fe values of the dFe. Figures were made using ODV (Schlitzer, 2020, https://odv.awi.de/en/home/).

CL-16 ( $-0.72 \pm 0.07$  %), which itself was a little lighter than the previous measurements at these depths from the "SaFe" station (30°N, 140°W), which is located further south in the eastern North Pacific (-0.6 %; Conway and John, 2015).

#### 4. Discussion

#### 4.1. Iron source estimation with aerosol $\delta^{56}$ Fe and other parameters

The total Fe concentration in the bulk over the North Pacific in this study (0.3–62.4 ng m $^{-3}$ ) was much lower than that observed in the aerosols collected at onshore sites in East Asia or North America (i.e., typically 100–3000 ng m $^{-3}$ ) (Var et al., 2000; Kanayama et al., 2002; Wu et al., 2007b; Mahowald et al., 2009), but was in a range similar to that in summer in the previous studies in the North Pacific (Buck et al., 2013; Schroth et al., 2017; Kurisu et al., 2021; Marsay et al., 2022), meaning that the samples in this study were collected under a typical condition of North Pacific summer.

The bulk EFs suggest that Fe and Mn, with EFs close to one, were mainly of crustal origins, whereas V, Ni, Cu, Zn, and Pb, with EFs higher than 10, were of anthropogenic origin (Figs. 3b and S4). Although the presence of anthropogenic Fe and Mn was not clear from the bulk EFs, the elevated EF values in finer particles for all the analyzed elements mean the enrichment of the anthropogenic components in fine particles compared with coarse particles.

This study observed the lowest  $\delta^{56}$ Fe values ever observed for marine aerosols (down to -2.16 ‰, Conway et al., 2019; Kurisu et al., 2021). Different Fe sources may be more clearly detected in size-fractionated sampling than in bulk sampling (Fig. 6). Strong correlations were found between the size-fractionated aerosol  $\delta^{56}$ Fe and the EF values of Fe and other anthropogenic trace elements, including Mn, Zn, Cd, and Pb, in the fine particles in the coastal regions of East Asia (samples A1 to A3) and western North America (samples A16 and A17, Figs. 9 and S11). These results confirmed that the negative  $\delta^{56}$ Fe values in the fine particles were indeed caused by the presence of the combustion sources of Fe emitted by high-temperature evaporation processes (Kurisu et al., 2016b, 2019; Conway et al., 2019) along with these anthropogenic elements mainly emitted from coal combustion, ferrous/nonferrous metal smelting, and incineration (Zhu et al., 2020a; Kajino et al., 2020). The

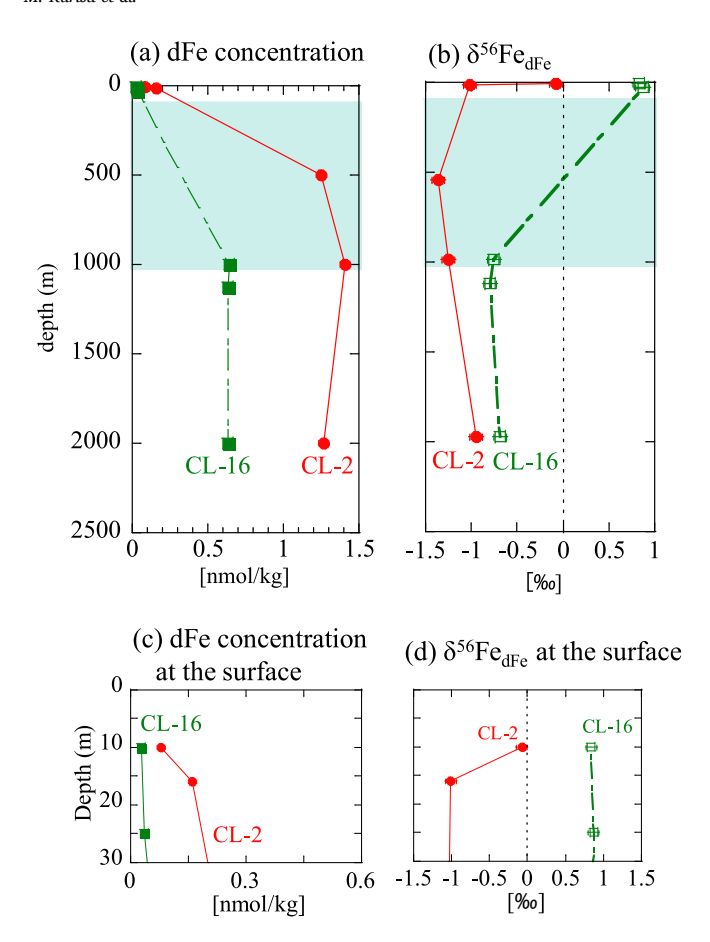


**Fig. 8.** Depth profiles at stations CL-2 and CL-16. (a) dFe concentrations and (b)  $\delta^{56}$ Fe of dFe. Expanded plot of the same data as in parts (a) and (b) are shown in (c) and (d). The blue-colored depth is the NPIW range (26.6–27.5  $\sigma_{\theta}$ ) at Station CL-2.

poor correlations between  $\delta^{56}$ Fe and the EFs of V or Cu suggested that the emission source of Fe with low  $\delta^{56}$ Fe was not necessarily related to the main V or Cu emission sources, such as ship emission, Cu smelting, and brake ware (Nriagu and Pacyna, 1988; Zhu et al., 2020a). The presence of combustion Fe is also suggested from the elevated ratio of water-soluble Fe to Al in the samples (Sakata et al., 2023) with low  $\delta^{56}$ Fe (Fig. S12), which was discussed in Supplementary Materials.

The EF plots of Cd and Pb against  $\delta^{56}$ Fe showed different slopes between the coastal regions of East Asia and western North America (Fig. 9c and d), indicating different characteristics of the anthropogenic components in the aerosol particles in these regions. The main Pb and Cd sources are coal and liquid fuel combustion, incineration, and ferrous/ non-ferrous metal smelting. Coal combustion is more dominant in East Asia, while nonferrous smelting is more dominant in North America (Zhu et al., 2020; McDuffie et al., 2021; Bai et al., 2023), which could cause the different  $\delta^{56}$ Fe and EF characteristics of the combustion aerosols in the two regions. The estimated  $\delta^{56}$ Fe signature of combustion Fe in East Asia was  $-4.3 \pm 0.4$  %, which was obtained based on the  $\delta^{56}$ Fe of water-soluble Fe in aerosol particles in suburban areas of Japan or the  $\delta^{56}$ Fe of particles collected near various emission sources (Kurisu et al., 2019), while -1.6 ‰ might be assumed as the value for North America based on the lowest  $\delta^{56}$ Fe value among water-soluble Fe observed in the North Atlantic when air masses were from North America (Conway et al., 2019). That said, Conway et al. (2019) did not sample western North American aerosols. Since the combustion  $\delta^{56}$ Fe signature may vary regionally, further studies on the endmember of combustion Fe are necessary.

In the pelagic regions and the Alaskan coastal regions, no good

correlations were observed between the size-fractionated aerosol  $\delta^{56} Fe$  and EF values of Mn, Fe, V, Cu, Zn, Cd, and Pb. Some high EF values were found with the  $\delta^{56} Fe$  values close to the crustal average, indicating that the air masses contained anthropogenic trace elements, such as V, Cu, Zn, Cd, and Pb (Figs. 8 and S12), but did not possess significant amounts of combustion Fe compared to the amount of crustal Fe. This was probably due to the absence of large-scale industrial activities in this region.

The origin of the  $\delta^{56}$ Fe values higher than the crustal average observed in the bulk and coarse particles in samples A5 and A6 (Fig. 6a and d) remains unclear. Such high  $\delta^{56}$ Fe values were also observed in the previous studies on the North and Equatorial Pacific (Labatut et al., 2014; Conway et al., 2019; Kurisu et al., 2021). Kurisu et al. (2021) discussed the possibilities of (i) another Fe source with high  $\delta^{56}$ Fe values and (ii) isotope fractionation during long-range transport. In the case of (i), different sources of mineral dust aerosols are not plausible explanation since there has been no report of mineral aerosol particles or loess with such high  $\delta^{56}$ Fe values (Beard et al., 2003; Majestic et al., 2009; Mead et al., 2013; Gong et al., 2017; Johnson et al., 2020; Wang et al., 2022). It is possible that these high  $\delta^{56}$ Fe values are derived from Fe in coal or oil residual ashes (emitted without evaporation) since their  $\delta^{56}$ Fe values ranges from -0.1 to +0.75 % (Mead et al., 2013; Kurisu et al., 2016a; Li et al., 2022). If (ii) isotope fractionation during long-range transport occurs, photochemical or acidification processes solubilize lighter Fe from each particle, and the remaining solid phase is enriched with heavy Fe, although it remains unclear if the separation of the liquid and solid phases does occur. Further studies are necessary to examine the source of this isotopically heavy Fe.

### 4.2. Influence of anthropogenic Fe on aerosol Fe solubility

The fractional Fe solubilities of the bulk aerosol particles obtained by the batch extraction (average:  $11.6\pm12.4$  %, SD, Fig. 3d) were higher than those of mineral aerosols on land at emission (i.e., typically  $0.1{\text -}1$ %; Schroth et al., 2009; Takahashi et al., 2011; Mahowald et al., 2018), but similar to those observed in marine North Pacific aerosols ( $8\pm7$  %; Buck et al., 2006; Buck et al., 2013, Kurisu et al., 2021, Sakata et al., 2022). This can be explained by the contribution of highly soluble combustion Fe and/or by atmospheric processing during transport. We discussed the controlling factor determining the Fe<sub>sol</sub>% in (i) the coastal regions of East Asia and western North America and in (ii) pelagic and Alaskan coastal regions separately.

### 4.2.1. In the coastal regions of East Asia and western North America

We obtained a strong correlation between the Fe<sub>sol</sub>% and the  $\delta^{56}$ Fe of the total (acid-digested) fraction in the size-fractionated aerosols of the coastal regions of East Asia and western North America (samples A1–A3, A16, and A17; Fig. 10). This study found a clearer relationship than those found in previous studies (Conway et al., 2019; Kurisu et al., 2021) because of the fine-size fractionated aerosol sampling. The correlation indicates the dominance of combustion Fe with low  $\delta^{56}$ Fe values as a soluble Fe source in the coastal regions of East Asia and western North America.

The preferential dissolution of combustion Fe in our samples was also indicated by the lower  $\delta^{56}$ Fe of the water-soluble fraction than the total Fe in the bulk aerosol particles (Fig. 6a), as was also shown in previous studies (Conway et al., 2019; Kurisu et al., 2021). The differences were especially large in the coastal regions of East Asia and western North America. It should be noted that it is possible that the partial dissolution of mineral Fe might release isotopically light Fe, as reported in several studies (Revels et al., 2015; Mulholland et al., 2021; Maters et al., 2022). However, we regard this effect to be small in our case because (i) the EF of Pb, which is indicative of the anthropogenic component, of the bulk aerosols is better correlated with the  $\delta^{56}$ Fe of water-soluble Fe than that of total Fe (Figs. S13a and b), and (ii) negative  $\delta^{56}$ Fe values of water-soluble Fe were observed when the  $\delta^{56}$ Fe values of the fine-size

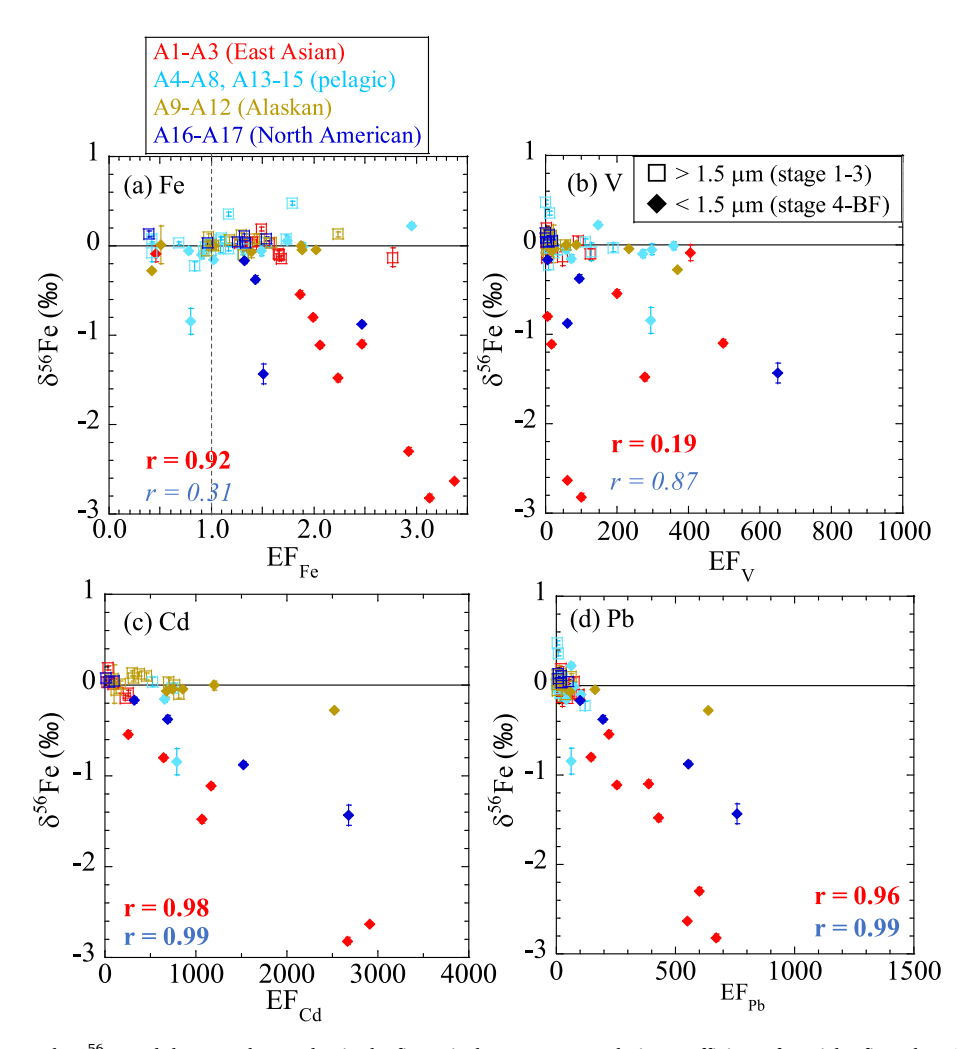


Fig. 9. Relationship between the  $\delta^{56}$ Fe and the EFs. The R value in the figure is the Pearson correlation coefficient of particles finer than 1.5  $\mu$ m of the western (red) and eastern (blue) coastal areas. See Table S6 for the other regions. Italicized letter means a p value larger than 0.05.

fractions were also negative (Fig. S13c). This indicates that the preferential dissolution of combustion Fe from fine particles was the predominant mechanism for the lower  $\delta^{56}\text{Fe}$  in the aerosol samples.

The high solubilities of the fine particles in these samples were related to the enrichment of highly soluble Fe species in the size-fractionated aerosol samples, such as Fe(III) sulfate, Fe(III) oxalate, and Fe(III) citrate (Fig. S14a). Iron (III) sulfate and Fe(III) oxalate are also found in anthropogenic aerosols on land, formed as a result of a reaction with sulfate and oxalate in the atmosphere (Li et al., 2017; Zhu et al., 2020). Although it is possible that Fe(III) sulfate was directly emitted from oil combustion (Schroth et al., 2009; Takahashi et al., 2013), this was not the case this time considering that the presence of Fe (III) sulfate was not related to the EF of V. Iron (III) citrate was observed in marine aerosols but not in lithogenic aerosol particles (Sakata et al., 2022). The combination of Fe isotope ratios and Fe speciation suggests that combustion Fe was altered to soluble chemical species, resulting in high fractional Fe solubilities.

#### 4.2.2. In the pelagic and Alaskan coastal regions

The samples from the pelagic and Alaskan coastal regions, where mineral aerosol Fe was dominant, sometimes showed much higher solubilities than the coastal regions of East Asia and western North America in spite of the fact that they did not contain combustion Fe with low  $\delta^{56}$ Fe (Fig. 10). In other words, the presence of combustion Fe cannot solely explain the high fractional Fe solubilities observed in the subarctic North Pacific, and that other effects, such as atmospheric processing,

increased  $Fe_{sol}$ %. The role of atmospheric processing was supported by a weak correlation between the [nss- $SO_4^2$ ]/[Total Fe] and  $Fe_{sol}$ % of the bulk aerosols (Fig. S14b), except for Sample A12, suggesting that the acidification processes (e.g., proton-promoted dissolution of Fe in mineral aerosols) during transport may have enhanced  $Fe_{sol}$ %. This is also supported by the enrichment of ferrihydrite compared with the mineral dust in China or Chinese desert sediments (Takahashi et al., 2011; Lu et al., 2017), as had been observed in previous studies as well (Kurisu et al., 2021; Sakata et al., 2022).

The reason for the especially high Fe<sub>sol</sub>% of Sample A12 near the Alaskan coast is unknown, but may be related to a specific aerosol composition. This sample showed a much higher Fesol% for the batch extraction (52 %) when compared to the flow-through extraction (17 %, Fig. 3d and S7b), indicating that Fe in this sample was contained in a form that gradually dissolved, rather than in an easily soluble form like Fe(III) sulfate or oxalate. Some possible sources are glacial flour dust and volcanic ash. Glacial flour dust contains a large proportion of "easily reducible" Fe (in this case Fe adsorbed on surface silicates) as a result of mechanical weathering of mineral materials (Schroth et al., 2009; Crusius et al., 2011; Koffman et al., 2021), which consequently could be more solubilized by atmospheric processing compared to Asian mineral dust. Volcanic ash is co-emitted with acidic gases, which enhances atmospheric processing (Ayris and Delmelle, 2012; Maters et al., 2016). These different sources of natural Fe derived from Alaska and Aleutian Islands could lead to a higher Fe<sub>sol</sub>% in Sample A12.

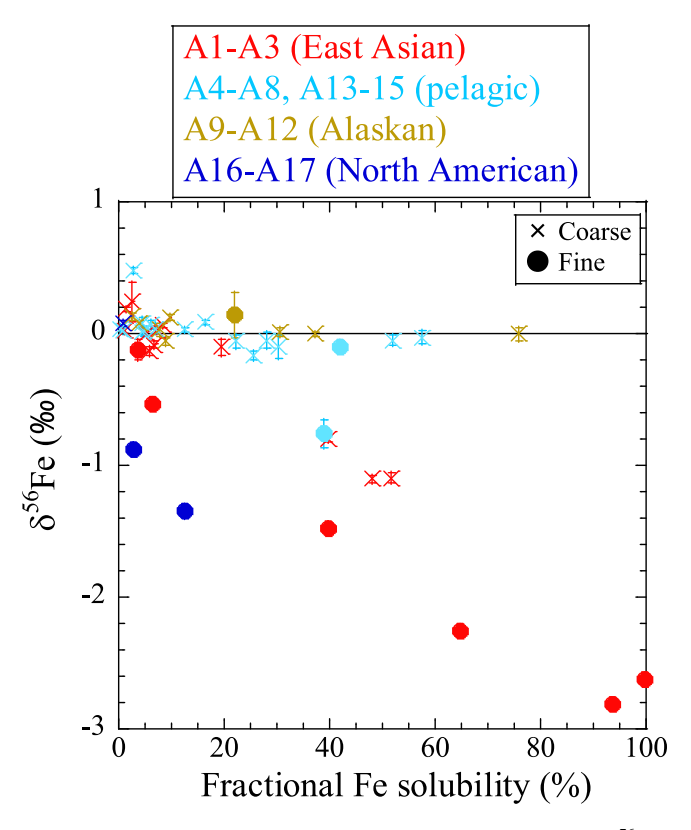


Fig. 10. Relationship between (a) the fractional Fe solubility and the  $\delta^{56}$ Fe of the total (acid-digested) Fe in the size-fractionated aerosol particles.

# 4.3. The contribution of combustion and natural Fe in the marine aerosol particles and surface seawater

The contribution of combustion Fe ( $f_{comb}$ ) in the marine aerosol particles was estimated as follows using the mixing equation:

$$\delta^{56} Fe = \delta^{56} Fe_{comb} \times f_{comb} + \delta^{56} Fe_{nat} \times (1 - f_{comb})$$

$$\tag{7}$$

where  $\delta^{56} Fe_{comb}$  and  $\delta^{56} Fe_{nat}$  are the representative  $\delta^{56} Fe$  values of combustion and crustal Fe, respectively. The  $\delta^{56} Fe_{crust}$  was assumed as +0.1 % (Beard et al., 2003; Johnson et al., 2003; Fitzsimmons and Conway, 2023), while the  $\delta^{56} Fe_{comb}$  was assumed as  $-4.3 \pm 0.4$  %, which was estimated using the observational results for combustion aerosols from Japan (Kurisu et al., 2019). As noted in Section 4.1, combustion Fe emitted from North America can have  $\delta^{56} Fe$  values different from those derived from our results for Japan and East Asia. We accounted for this variability by estimating the contribution in the coastal region of western North America (samples A16 and A17) by assuming  $\delta^{56} Fe_{comb}$  as -1.6 %, as reported by Conway et al. (2019). We assumed samples with  $\delta^{56} Fe$  higher than +0.1 % to be of crustal origin.

The combustion Fe contribution in the bulk aerosols was 0–13 %, with the highest contribution found in the coastal region of East Asia (Table 1, Fig. S15). The contribution in the coastal region of western North America was 3–5 % with the assumed of  $\delta^{56} \text{Fe}_{\text{comb}}$  value of -4.3 ‰, whereas it was higher (8–14 %) with the  $\delta^{56} \text{Fe}_{\text{comb}}$  of -1.6 ‰. The combustion Fe in the fine fraction (<0.95  $\mu\text{m}$ ) of the particles was significantly higher than the bulk, with 18–51 % found in the coastal regions of East Asia and 22–33 % (or 57–85 % with the  $\delta^{56} \text{Fe}_{\text{comb}}$  of -1.6 ‰) in western North America. By comparison, the pelagic and Alaskan coastal regions showed only a small contribution of combustion Fe (0–4 % in the bulk) (Table 1). Although some samples contained a relatively high fraction of combustion Fe in fine particles (up to 20 % in Sample A5), most samples contained only a small fraction of combustion Fe (less than 5 %), even in fine particles.

**Table 1**Contribution of combustion Fe in marine aerosols (%).

	In total (acid digested)		In soluble
	Bulk (all the size fraction)	Fine (<0.95 μm)	Bulk (all the size fraction)
A1	11	51	31
A2	13	34	45
A3	4	18	13
A4	1	5	5
A5	0	20	5
A6	0	n.d.	7
A7	n.d.	n.d.	n.d.
A8	0	n.d.	14
A9	3	9	4
A10	1	0	0
A11	0	3	6
A12	1	2	0
A13	n.d.	n.d.	n.d.
A14	4	n.d.	5
A15	0	1	0
A16	5 (14)	33 (85)	20 (53)
*			
A17	3 (8)	22 (57)	16 (42)
*			

 $<sup>^*</sup>$  The value in the parenthesis was estimated by assuming  $\delta^{56}\text{Fe}$  of combustion Fe as -1.6 ‰. n.d.: not determined.

The combustion Fe contribution was compared with that in western Pacific in the summer of 2014 (Kurisu et al., 2021). Both studies showed that a high combustion Fe contribution of over 10 % in fine particles (finer than 2.5 µm in Kurisu et al. (2021)) is found within approximately 3000 km from the Japanese coast, whereas combustion Fe is negligible in pelagic regions, even in the fine particle fraction. Kurisu et al. (2021) estimated a higher combustion Fe contribution in the bulk aerosols (up to 21 %) than that obtained from the similar locations in this work (Fig. S15). This difference is mainly caused by the higher natural Fe concentrations in this study. For example, the natural and combustion Fe concentrations in Sample A2 calculated from the combustion Fe contribution (13 %) and the total Fe concentration were 20.5 and 3.04 ng m<sup>-3</sup>, respectively, which are both higher than those in the similar region in the summer of 2014 (7.48 and 1.61 ng m<sup>-3</sup>, respectively), when the combustion Fe contribution was 18 %. This result implies that the combustion Fe fractions partly depend on the large variety of natural aerosol input to the East Asian coastal region.

The calculation was also applied for the  $\delta^{56}\mbox{Fe}$  of the water-soluble fractions of the samples. The average contribution was 13-45 % in the coastal regions of East Asia and 16-20 % (or 42-53 % with the assumption of  $\delta^{56} Fe_{comb}$  as -1.6 %) in western North America, depicting values that were up to 10 times higher than those in the total Fe in the bulk. This indicates that the combustion Fe contribution to the dFe flux was as large as that of Fe in mineral dust in the coastal regions. In contrast, the combustion Fe contribution to the water-soluble aerosol phase was up to 14 % (average: 5 %) in the pelagic and Alaskan coastal regions. This is an important observational result because atmospheric chemical transport models sometimes provide a larger estimate of the combustion Fe contribution during summer (10-40 % on global average, Myriokefalitakis et al., 2018). Although a proper  $\delta^{56}$ Fe<sub>comb</sub> evaluation is necessary in the future considering that the results largely depend on the  $\delta^{56}$ Fe<sub>comb</sub>, these observational results can effectively be used for a model-based estimation (Conway et al., 2019; Kurisu et al., 2021).

Atmospheric water-soluble Fe (wet + dry) deposition flux to the surface seawater  $F_{sol}$  was roughly estimated based on the following equation:

$$F_{sol} = C_{solFe} \times V \tag{8}$$

where  $C_{solFe}$  is the water-soluble aerosol concentration of natural and combustion Fe, in which the fraction of the natural and combustion Fe was calculated from the  $\delta^{56}$ Fe of water-soluble Fe. V is the wet + dry deposition rate, assumed as  $1764 \pm 261$  m day  $^{-1}$ , and estimated from

the surface ocean inventory of  $^7\text{Be}$  in the North Pacific (Marsay et al., 2022). The calculated natural Fe deposition flux ranged from 1.7-129 nmol Fe m $^{-2}$  day $^{-1}$ , with the highest flux found in the coastal region of East Asia and the lowest flux in the pelagic region (Table S7). The flux in the pelagic region (up to 21 nmol Fe m $^{-2}$  day $^{-1}$ ) was in a similar range to that in previous reports in the North Pacific in clean seasons without large dust events (Table S7; Uematsu et al., 1983; Measures et al., 2005; Marsay et al., 2022). These results indicated that the aerosol particles in this study were collected under a typical environment in the North Pacific during summer. The combustion Fe fluxes were 1.6–58 nmolFe m $^{-2}$  day $^{-1}$  in the coastal region of East Asia (samples A1–A3) and 1.2–1.5 (or 3.0–3.9 with the  $\delta^{56}$ Fecomb of -1.6%) nmolFe m $^{-2}$  day $^{-1}$  in western North America (samples A16 and 17), respectively.

The atmospheric water-soluble Fe deposition flux was compared with the upward dFe flux from the intermediate depth (500 m) to the surface (over 100 m, 0.1-17 nmolFe m $^{-2}$  day $^{-1}$ ) in the same regions estimated from the measured vertical diffusivity and the dFe gradient reported by Nishioka et al. (2020). The atmospheric Fe deposition was comparable to or larger than the upward dFe flux in summer (Table S8). This indicates that the atmospheric deposition, including combustion Fe is an important dFe source in summer, even in pelagic regions.

It should be noted that the atmospheric deposition fluxes and the fraction of each source are highly variable on seasonal and interannual time scales. The results obtained in this study in summer are a 'snapshot', we note that the deposition fluxes could vary during other seasons and also between summers.

# 4.4. Isotopic composition of dissolved Fe at intermediate depths of the North Pacific

The upward Fe supply from the deeper seawater depth is another important dFe source, as noted earlier. Our study is the first to reveal the low  $\delta^{56}$  Fe<sub>dFe</sub> signals (i.e., as low as -1.4 %) at intermediate depths of the western subarctic North Pacific (Fig. 8). dFe at these intermediate depths is supplied either by internal cycling due to remineralization (organic particle decomposition) of vertically transported particles, or by external sources mainly horizontally transported from the Sea of Okhotsk and the continental margin around Kamchatka via NPIW, the influence of which is much larger in the western North Pacific (Lam and Bishop, 2008; Nishioka and Obata, 2017; Nishioka et al., 2020, 2021; Kondo et al., 2021). Considering both the elevated dFe concentration and the very light  $\delta^{56}$ Fe<sub>dFe</sub> at Station CL-2 (-1.25 % to -1.36 %) compared to CL-16, these signals can be attributed to the presence of external dFe supplied via NPIW. dFe is discharged from the sediment porewaters at the bottom of the continental shelf caused by the release of Fe(II) from reducing environments (reductive dissolution), perhaps rapidly oxidized to Fe(III), and then transported at a long range as dFe (III) after complexed to organic ligands (Cid et al., 2011; Nishioka et al., 2014, 2021; John et al., 2018; Kondo et al., 2021). Reductive dissolution is now well characterized in both sediment porewaters and bottom waters as producing isotopically light  $Fe^{2+}$ , with signatures of -3.45 to -0.3 % that can be maintained some distance away from the source (e.g. Homoky et al., 2009; Severmann et al., 2010; John, 2012; Hunt et al., 2022). Therefore, the low  $\delta^{56}Fe_{dFe}$  signals in this study probably originate from dFe discharged by reductive dissolution.

At Station CL-16, the  $\delta^{56}$ Fe<sub>dFe</sub> below 200 m was found to be approximately -0.7 %, which was higher than that at Station CL-2, but very similar to that of the nearby SAFe station (-0.6 %; Conway and John, 2015). This isotopically light signature was indicative of the influence of a sedimentary margin source, which was consistent with previous studies suggesting that the isotopically light Fe at 500-2500 m at SAFe could be attributed to the transport of the sediment-derived Fe through the North Pacific oxygen minimum zone from the North American (Californian) margin and the transport of light Fe in the subsurface waters within NPIW (Johnson et al., 1997; Conway and John, 2015). At the location of Station CL-16, the sediment-derived Fe can also

be sourced from the local Canadian or Alaskan margins (Johnson et al., 2005; Schoenberg and Von Blanckenburg, 2005; Cullen et al., 2009). A more detailed iron isotope investigation of such sediment transport is beyond the scope of the limited dataset we have herein, but is a goal of the GEOTRACES sections GP15 and GP02 (Nishioka et al., 2020; Fitzsimmons and Conway, 2023). As to why the  $\delta^{56} Fe_{dFe}$  at Station CL-16 was not as light as that in Station CL-2 (Fig. 8a and b), the lower dFe concentrations at Station CL-16 suggest that the sediment-derived Fe was relatively less abundant at the distal end of any plumes compared with the Station CL-2 in the west. Remineralized Fe is also likely to play a role in influencing the  $\delta^{56} Fe_{dFe}$  here, although the isotope signature of Fe released into this pool remained unclear (Fitzsimmons and Conway, 2023).

# 4.5. Comparison of $\delta^{56}$ Fe of surface seawater and aerosol particles

The  $\delta^{56}$ Fe<sub>dFe-surface</sub> at 10 m depth was compared to those of the watersoluble aerosol particles collected in a similar region considering that the  $\delta^{56}$ Fe of the water-soluble fraction may reflect the aerosol contribution to the seawater dFe. The  $\delta^{56}$ Fe values of the aerosols were the concentration-weighted average of the two nearest stations across the seawater sampling site. The surface seawater showed  $\delta^{56}$ Fe<sub>dFe-surface</sub> values up to +1.5 % higher than the water-soluble fraction of the aerosol particles in most regions (Fig. 11a). A particularly large difference was observed in the pelagic regions where the Fe concentrations of the surface seawater were low (less than 0.05 nmol kg<sup>-1</sup>, Fig. 8a and b). By contrast, the difference was small at Station CL-2 in the western North Pacific and CL-14 near the Alaskan coast. The  $\delta^{56}$ Fe<sub>dFe-surface</sub> was even higher than the total fraction of the aerosol particles in most regions. Therefore, the  $\delta^{56}$ Fe of the aerosols were not directly reflected in the surface seawater. Other processes or sources must be considered to explain the  $\delta^{56}$ Fe<sub>dFe-surface</sub>.

The upward dFe supply from the intermediate depth cannot explain the high  $\delta^{56} Fe_{dFe-surface}$  because the  $\delta^{56} Fe_{dFe}$  at the intermediate depth was lower than the  $\delta^{56} Fe$  of the aerosol particles (Figs. 6a and 8b). In addition, the detailed depth profile of the dFe concentration at the same cruise reported by Nishioka et al. (2020) also showed that surface seawater (10 m) dFe concentrations were similar or higher than the subsurface depths (20–50 m), indicating a limited Fe supply from the intermediate depth to the surface seawater (10 m).

A correlation existed between the  $\delta^{56} Fe_{dFe-surface}$  and the logarithm of the dFe concentration, except for Station CL-14 (Fig. 11b). This means that (i) the  $\delta^{56} Fe_{dFe-surface}$  can mainly be explained by a single Rayleigh fractionation process (best-fit fractionation factor ( $\alpha$ ): 0.9993  $\pm$  0.0001); (ii) the surface seawater in these regions and seasons is a closed or semi-closed system for the dFe; and (iii) the original dFe concentration and the  $\delta^{56} Fe$  before the fractionation are almost consistent and varied within the scatter of the data.

Several possible internal cycling processes might play a role in modifying the  $\delta^{56}$ Fe<sub>dFe</sub> of the surface seawater, including biological uptake, ligand complexation, scavenging, and recycling, although the exact fractionations associated with these mechanisms remain to be poorly constrained (Fitzsimmons and Conway, 2023). Prior studies on the North Atlantic also reported  $\delta^{56} Fe_{dFe-surface}$  to be up to +0.7 % higher than the  $\delta^{56}\mbox{Fe}$  signature of mineral dust, which is the largest Fe source in the region (John and Adkins, 2012; Conway and John, 2014), while both water soluble and bulk aerosol Saharan mineral dust was crustal (+0.1 %; Conway et al., 2019). These studies attributed this fractionation to the ligand-mediated particle dissolution (e.g., heavier Fe preferentially combined with ligands, and uncomplexed light dFe is preferentially scavenged). However, in the case of the North Pacific in this work, the dissolved-particle buffering of the  $\delta^{56}$ Fe<sub>dFe-surface</sub> is unlikely to be the main reason for the high  $\delta^{56}\text{Fe}_{\text{dFe-surface}}$  because Fe had almost been depleted at the surface (less than 0.1 nmol kg<sup>-1</sup>), when compared to the dusty subtropical North Atlantic (0.3–0.9 nmol kg<sup>-1</sup> in pelagic regions).

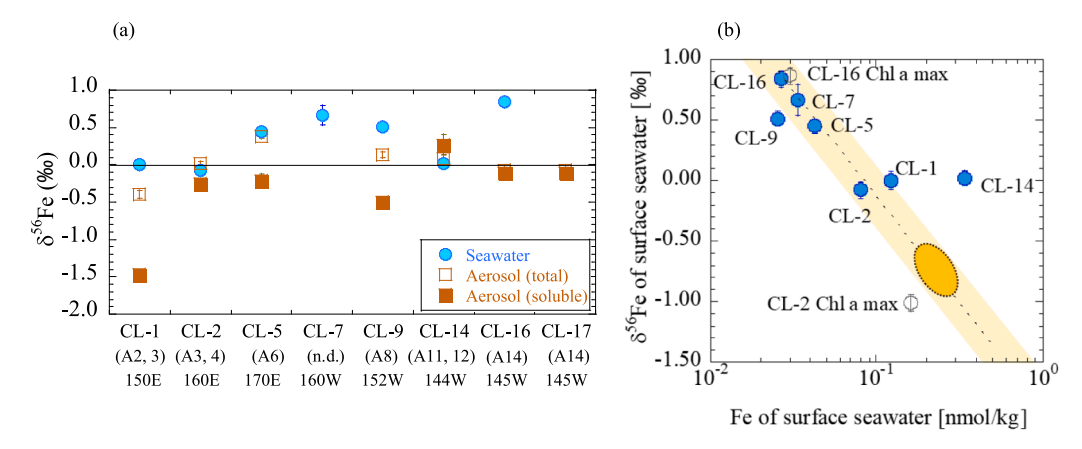


Fig. 11. (a) Comparison of the  $\delta^{56}$ Fe of dFe in the surface seawater and bulk aerosol particles. Some of the aerosol values were the concentration-weighted average of the two nearest stations across the seawater sampling point. (b) Scatter plot of the concentration and the  $\delta^{56}$ Fe of dFe of the surface seawater (blue, 10 m) and Chl  $\alpha$  maximum (gray). The yellow range and the orange circle indicate the error range of the scatter (2 $\sigma$ ) and the estimated original Fe composition before the biological uptake, respectively.

We regard isotope fractionation caused by biological uptake as being more important in this case, because the Chl a maximum was at the surface in the North Pacific, and primary production was more influential in driving down dFe in the Fe-limited subarctic North Pacific than in the subtropical Atlantic. This had also been suggested by global ocean biogeochemical models that found source signatures to be strongly overprinted by uptake fractionation in this region (König et al., 2022). Previous observational studies showed that the  $\delta^{56}$ Fe<sub>dFe</sub> became higher after biological uptake (  $\Delta^{56} Fe_{dFe\text{-}phytoplankton}$  : +0.13 to +0.60 %; Radic et al., 2011; Ellwood et al., 2015), Similar fractionations and  $\alpha$  values were recently reported within an eddy or a polynya in the Southern Ocean (0.997-0.999, Ellwood et al., 2020; Sieber et al., 2021; Tian et al., 2023). These studies also pointed to the combined effect of biological uptake along with scavenging, and complexation (Ellwood et al., 2020; Sieber et al., 2021) in setting the heavy  $\delta^{56}$ Fe<sub>dFe-Surface</sub> in Southern Ocean waters. Overall, our results are consistent with the abovementioned findings. It is notable that a clear signal of isotope fractionation is also seen in the surface of the North Pacific, where dFe concentration is low enough to be mostly Fe-limited, which is most likely related to biological activity.

The closed or semi-closed system suggests that the new dFe supply was small compared with the concentration decline due to the biological uptake. Although the atmospheric Fe deposition flux was comparable to upward Fe flux from the intermediate depth, their fluxes were not high enough to change surface dFe and  $\delta^{56}\text{Fe}_{\text{dFe-surface}}.$  The surface dFe is likely replenished (and  $\delta^{56}$ FedFe reset) during winter and spring by ocean vertical mixing or a large atmospheric deposition (Nishioka et al., 2007; Tagliabue et al., 2014) and then utilized in summer. Since the dFe concentration at the subarctic North Pacific surface becomes as high as 0.2–0.3 nmol kg<sup>-1</sup> in winter/spring (Nishioka et al., 2021), if we assume this range to be the original dFe concentration, the original  $\delta^{56}$ Fe<sub>dFe</sub> will be -0.6 to -0.9 % based on the relationship depicted in Fig. 11b, which was probably obtained by mixing Fe from aerosol particles (both natural and combustion) and from the intermediate depths. This would be consistent with the findings of Pinedo-González et al. (2020) who found  $\delta^{56}$ Fe<sub>dFe</sub> as low as -0.6 % associated with 0.3–0.4 nmol kg<sup>-1</sup> in early summer in the subtropical North Pacific, and the model of König et al. (2022), who modelled the high seasonal variability in the surface δ<sup>56</sup>Fe<sub>dFe</sub> across the region. However, more observation of the concentration and the  $\delta^{56}$ Fe of seawater and aerosols during winter will clearly lead to a more quantitative assessment of the Fe fluxes from different sources.

Station CL-14 was out of the correlation line in Fig. 11b; it had  $\delta^{56}Fe_{dFe}$  close to 0.0 % and showed higher dFe concentration than the other samples. Station CL-14 was very close to the shore and largely

influenced by the Fe discharge from Copper River in summer (Crusius et al., 2017; Wong et al., 2022). This was also suggested by the reported near-crustal  $\delta^{56}$ Fe<sub>dFe</sub> in the glacial tributary systems of Copper River (Schroth et al., 2011). The atmospheric deposition contribution to dFe was small in this season compared to the river discharge (Crusius et al., 2011).

Interestingly, the  $\delta^{56} Fe_{dFe}$  at 10 m was 1 % higher than that at the Chl a maximum (16 m) depth at Station CL-2 (associated with a 50 % drop in dFe), whereas a small difference was found between 10 m and Chl a maximum (25 m) depths at Station CL-16 (similar dFe). When these two  $\delta^{56}$ Fe<sub>dFe</sub> values at Chl a maximum were included in the scatter plot in Fig. 11b, the value at CL-16 was within the scatter of the surface (10 m) data, indicating that it can be explained by a similar isotope fractionation, i.e. biological uptake. However, the  $\delta^{56}$ Fe<sub>dFe</sub> value at Chl a maximum at Station CL-2 was not on the correlation line, suggesting that the dFe source or the dFe removal processes at the surface and the Chl a maximum at Station CL-2 may be different, despite the observation that winter mixing results in a homogeneous Fe concentrations (Nishioka et al., 2007) and probably in homogeneous  $\delta^{56}$ Fe<sub>dFe</sub> at the mixed layer in winter ( $\sim$ 100 m). As such, the  $\delta^{56}$ Fe<sub>dFe</sub> differences may have developed after the mixed layer shallowed to 10 m and might be related to the biological uptake with a different fractionation factor, particle scavenging, or addition of atmospheric aerosols to the mixed layer (10m). We currently do not have sufficient information to determine which process might be driving this change, but seasonal observation in the region will help answer this question.

# 4.6. Implication for understanding Fe cycles in the atmosphere and surface ocean

Our study demonstrated the applicability of Fe stable isotope ratios for aerosol Fe source identification in coastal and pelagic regions of the North Pacific, which can be applied more broadly. A notable finding of this study is that including consideration of multiple size-fractions of aerosol particles during sampling allows for identification of the presence of combustion Fe in fine particles, which can be masked in bulk aerosol particles due to its low abundance compared with natural Fe in coarse particles. Use of size-fractionated aerosol data also enabled us to discuss in detail the effect of Fe source differences in determining fractional Fe solubilities and chemical composition.

Our study provides insight into anthropogenic combustion Fe supply to the North Pacific during summer, which is important for forcing dust models. We found that while combustion Fe was abundant in the coastal regions of the North Pacific, the contribution of combustion Fe was much more minor in pelagic regions and Alaskan coastal regions. Our

observation was conducted in summer when atmospheric Fe concentrations were typically low. In high dust seasons in spring, larger amount of natural and anthropogenic aerosol particles from East Asia could be transported further to the pelagic regions and likely change the contribution of combustion Fe in aerosol particles. This requires further research to understand seasonal variability.

By comparing the  $\delta^{56}$ Fe of aerosol particles and surface seawater near-simultaneously, we also reinforced the idea that Fe isotope fractionation needs to be taken into account when estimating any Fe sources in the surface ocean, as also suggested by a model study (König et al., 2022). The finding that isotope fractionation by phytoplankton uptake is a dominant mechanism that determines the  $\delta^{56}$ Fe of surface seawater in a wide area of the Fe-limited open ocean in the North Pacific has implications for using surface  $\delta^{56}$ Fe as a direct tracer of Fe sources anywhere in the oceans, especially where Fe is limiting or dFe supplies are low. Conversely, it is possible that the  $\delta^{56}$ Fe of source materials might be reflected in surface seawater  $\delta^{56}$ Fe in regions and during seasons in which Fe supply is much larger than Fe consumption. Further near-simultaneous sampling of seawater and source addition of Fe (and source materials) should provide information on Fe cycles in the surface ocean in such areas and seasons, and is needed.

#### 5. Conclusion

The Fe isotope ratios of the aerosol particles across the subarctic North Pacific in summer revealed that up to 45 % of the atmospheric water-soluble Fe was sourced from high-temperature combustion in the coastal regions of East Asia and western North America. By contrast, the combustion Fe contribution to the aerosols was much more limited in the pelagic regions of the North Pacific and near the Alaskan coastal regions, where Fe in mineral dust was dominant in both the coarse and fine particles. The fractional Fe solubilities of the bulk aerosol particles across the North Pacific were higher than the mineral dust, which can partly be explained by the presence of combustion Fe in the coastal regions, with the atmospheric processing of mineral dust deemed to be more important in the other regions.

The surface seawater in the North Pacific in summer did not simply reflect total or water-soluble aerosol  $\delta^{56} Fe$ . The small external Fe fluxes from the atmosphere and the upwelling from the intermediate depths of the ocean play only a limited role in setting the dFe and  $\delta^{56} Fe_{dFe}$  in the surface seawater during summer. Instead, the isotope fractionation driven by the biological uptake of Fe was found to be the main process. We predict herein that the Fe supply increases in other seasons due to the winter vertical mixing and the increased aerosol deposition in spring, and that, during these seasons, the  $\delta^{56} Fe$  of the sources may be more clearly reflected in the surface seawater prior to the internal cycling dominating fractionation during summer. Thus, the seasonal  $\delta^{56} Fe$  measurements will contribute to a better understanding of the Fe sources in the atmosphere and the surface ocean, with implications for improving the accuracy of global biogeochemical models.

#### CRediT authorship contribution statement

Minako Kurisu: Conceptualization, Data curation, Formal analysis, Funding acquisition, Investigation, Methodology, Project administration, Resources, Validation, Visualization, Writing – original draft, Writing – review & editing. Kohei Sakata: Conceptualization, Investigation, Methodology, Writing – review & editing. Jun Nishioka: Investigation, Methodology, Validation, Writing – review & editing. Hajime Obata: Investigation, Methodology, Resources, Validation, Writing – review & editing. Tim M. Conway: Funding acquisition, Investigation, Methodology, Resources, Validation, Writing – review & editing. Matthias Sieber: Investigation, Writing – review & editing. Katsuhiko Suzuki: Methodology, Resources, Writing – review & editing. Teruhiko Kashiwabara: Methodology, Resources, Writing – review & editing.

**Sayuri Kubo:** Investigation, Writing – review & editing. **Makoto Takada:** Investigation, Writing – review & editing. **Yoshio Takahashi:** Conceptualization, Funding acquisition, Investigation, Project administration, Resources, Supervision, Writing – review & editing.

### Declaration of competing interest

The authors declare that they have no known competing financial interests or personal relationships that could have appeared to influence the work reported in this paper.

# Data availability

Data are available through Mendeley Data at https://doi.org/10.17632/p566r8vp7c.1.

# Acknowledgements

We appreciate the crew and scientists on the KH-17-3 cruise. This study was supported by Cooperative Research Program of Atmosphere and Ocean Research Institute, The University of Tokyo (Research Vessel Hakuho-maru, JURCAOSSH17-09). XAFS analysis was conducted with the approval of KEK-PF (2018G575, 2018G089, 2019G093, and 2021G123). We thank Ethan Goddard and Brent Summers for technical assistance at USF. This work was supported by the JSPS KAKENHI Grant Numbers 21K17886 and 17J06716 and Graduate Research Abroad in Science Program by the Univ. of Tokyo (to MK). YT acknowledges funding support from JSPS KAKENHI Grant Numbers 23H02303, 22H00166, 22KK0166, and 21H03585. TC acknowledges funding support from the US National Science Foundation (OCE-1829643 and OCE-1737136), and the University of South Florida. The International GEO-TRACES program is possible in part thanks to the support from the U.S. National Science Foundation (Grant OCE-2140395) to the Scientific Committee on Oceanic Research (SCOR). This paper also contributes to the science plan of the Surface Ocean-Lower Atmosphere Study (SOLAS), which is partially supported by the U.S. National Science Foundation (Grant OCE-1840868) via the Scientific Committee on Oceanic Research (SCOR).

### Appendix A. Supplementary material

The method section contains aerosol filter preparation method, analytical methods for the seawater salinity, nutrient concentration, and Chl a, and the flow-through extraction method. Supplementary results and discussion include the comparison of  $\delta^{56}$ Fe and [d-Fe]/[d-Al] in size-fractionated aerosols and the distinction of Fe-limited regions by the ratio of dFe and nitrate + nitrite. It also includes supplementary figures on the accuracy of the isotope analysis (Fig. S1), the backward trajectory (Fig. S2), aerosol data, such as trace element concentrations, water-soluble Fe concentrations, and Fe species (Figs. S3-S8), surface seawater [dFe]/[NO<sub>3</sub> + NO<sub>2</sub>] distributions (Fig. S9), hydrological parameters of seawater (Fig. S10), relationships between aerosol  $\delta^{56}$ Fe and other parameters (Figs. S11-S13), relationships between aerosol fractional Fe solubility and other parameters (Fig. S14), and the fraction of combustion Fe in total bulk aerosol samples (Fig. S15). Supplementary tables include aerosol sampling information (Table S1), trace element concentrations of reference materials (Table S2), blank concentrations of aerosol sampling filters (Table S3), the  $\delta^{56}$ Fe of seawater samples and aerosols (Tables S4 and S5), correlation coefficients between the aerosol δ<sup>56</sup>Fe and enrichment factors (Table S6), deposition flux of watersoluble aerosol Fe (Table S7), and comparison of dFe fluxes from the atmosphere and the intermediate water (Table S8). Supplementary material to this article can be found online at https://doi.org/10.1016/j. gca.2024.06.009.

#### References

- Abadie, C., Lacan, F., Radic, A., Pradoux, C., Poitrasson, F., 2017. Iron isotopes reveal distinct dissolved iron sources and pathways in the intermediate versus deep Southern Ocean. Proc. Natl. Acad. Sci. 114, 858–863.
- Ayris, P., Delmelle, P., 2012. Volcanic and atmospheric controls on ash iron solubility: a review. Phys. Chem. Earth 45–46, 103–112.
- Bai, X., Tian, H., Zhu, C., Luo, L., Hao, Y., Liu, S., Guo, Z., Lv, Y., Chen, D., Chu, B., Wang, S., Hao, J., 2023. Present knowledge and future perspectives of atmospheric emission inventories of toxic trace elements: a critical review. Environ. Sci. Technol. 57, 1551–1567.
- Beard, B.L., Johnson, C.M., Skulan, J.L., Nealson, K.H., Cox, L., Sun, H., 2003.
  Application of Fe isotopes to tracing the geochemical and biological cycling of Fe. Chem. Geol. 195, 87–117.
- Boyd, P.W., Jickells, T., Law, C.S., Blain, S., Boyle, E.A., Buesseler, K.O., Coale, K.H., Cullen, J.J., de Baar, H.J.W.W., Follows, M., Harvey, M., Lancelot, C., Levasseur, M., Owens, N.P.J.J., Pollard, R., Rivkin, R.B., Sarmiento, J., Schoemann, V., Smetacek, V., Takeda, S., Tsuda, A., Turner, S., Watson, A.J., 2007. Mesoscale iron enrichment experiments 1993–2005: synthesis and future directions. Science 315, 612–617.
- Buck, C.S., Landing, W.M., Resing, J.A., Lebon, G.T., 2006. Aerosol iron and aluminum solubility in the northwest Pacific Ocean: results from the 2002 IOC cruise. Geochem. Geophys. Geosyst. 7, 1–21.
- Buck, C.S., Landing, W.M., Resing, J., 2013. Pacific Ocean aerosols: deposition and solubility of iron, aluminum, and other trace elements. Mar. Chem. 157, 117–130.
- Chen, H., Laskin, A., Baltrusaitis, J., Gorski, C.A., Scherer, M.M., Grassian, V.H., 2012. Coal fly ash as a source of iron in atmospheric dust. Environ. Sci. Technol. 46, 2112–2120.
- Ciais, P., Sabine, C., Bala, G., Bopp, L., Brovkin, V., Canadell, J., Chhabra, A., DeFries, R., Galloway, J., Heimann, M., Jones, C., Le Quéré, C., Myneni, R.B., Piao, S., Thornton, P., 2014. Carbon and other biogeochemical cycles. In: Climate Change 2013 The Physical Science Basis. Cambridge University Press, pp. 465–570.
- Cid, A.P., Urushihara, S., Minami, T., Norisuye, K., Sohrin, Y., 2011. Stoichiometry among bioactive trace metals in seawater on the Bering Sea shelf. J. Oceanogr. 67, 747–764.
- Conway, T.M., Hamilton, D.S., Shelley, R.U., Aguilar-Islas, A.M., Landing, W.M., Mahowald, N.M., John, S.G., 2019. Tracing and constraining anthropogenic aerosol iron fluxes to the North Atlantic Ocean using iron isotopes. Nat. Commun. 10, 2628.
- Conway, T.M., John, S.G., 2014. Quantification of dissolved iron sources to the North Atlantic Ocean. Nature 511, 212–215.
- Conway, T.M., John, S.G., 2015. The cycling of iron, zinc and cadmium in the North East Pacific Ocean insights from stable isotopes. Geochim. Cosmochim. Acta 164, 262–283.
- Conway, T.M., Rosenberg, A.D., Adkins, J.F., John, S.G., 2013. A new method for precise determination of iron, zinc and cadmium stable isotope ratios in seawater by doublespike mass spectrometry. Anal. Chim. Acta 793, 44–52.
- Conway, T.M., John, S.G., Lacan, F., 2016. Intercomparison of dissolved iron isotope profiles from reoccupation of three GEOTRACES stations in the Atlantic Ocean. Mar. Chem. 183, 50–61.
- Crusius, J., Schroth, A.W., Gassó, S., Moy, C.M., Levy, R.C., Gatica, M., 2011. Glacial flour dust storms in the Gulf of Alaska: hydrologic and meteorological controls and their importance as a source of bioavailable iron. Geophys. Res. Lett. 38, L06602.
- Crusius, J., Schroth, A.W., Resing, J.A., Cullen, J., Campbell, R.W., 2017. Seasonal and spatial variabilities in northern Gulf of Alaska surface water iron concentrations driven by shelf sediment resuspension, glacial meltwater, a Yakutat eddy, and dust. Glob. Biogeochem. Cycles 31, 942–960.
- Cullen, J.T., Chong, M., Ianson, D., 2009. British Columbian continental shelf as a source of dissolved iron to the subarctic northeast Pacific Ocean. Glob. Biogeochem. Cycles 23, 1–12.
- Dauphas, N., John, S.G., Rouxel, O., 2017. Iron isotope systematics. Rev. Mineral. Geochem. 82, 415–510.
- Duce, R.A., Tindale, N.W., 1991. Atmospheric transport of iron and its deposition in the ocean. Limnol. Oceanogr. 36, 1715–1726.
- Duce, R.A., Unni, C.K., Ray, B.J., Prospero, J.M., Merrill, J.T., 1980. Long-range atmospheric transport of soil dust from Asia to the tropical North Pacific: temporal variability. Science 209, 1522–1524.
- Ellwood, M.J., Hutchins, D.A., Lohan, M.C., Milne, A., Nasemann, P., Nodder, S.D., Sander, S.G., Strzepek, R., Wilhelm, S.W., Boyd, P.W., 2015. Iron stable isotopes track pelagic iron cycling during a subtropical phytoplankton bloom. Proc. Natl. Acad. Sci. 112, E15–E20.
- Ellwood, M.J., Strzepek, R.F., Strutton, P.G., Trull, T.W., Fourquez, M., Boyd, P.W., 2020. Distinct iron cycling in a Southern Ocean eddy. Nat. Commun. 11, 825.
- Falkowski, P.G., Barber, R.T., Smetacek, V., 1998. Biogeochemical controls and feedbacks on ocean primary production. Science 281, 200–206.
- Fitzsimmons, J.N., Conway, T.M., 2023. Novel insights into marine iron biogeochemistry from iron isotopes. Ann. Rev. Mar. Sci. 15, 383–406.
- Fujiki, T., Hosoda, S., Harada, N., 2022. Phytoplankton blooms in summer and autumn in the northwestern subarctic Pacific detected by the mooring and float systems. J. Oceanogr. 78, 63–72.
- Gong, Y., Xia, Y., Huang, F., Yu, H., 2017. Average iron isotopic compositions of the upper continental crust: constrained by loess from the Chinese Loess Plateau. Acta Geochim. 36, 125–131.
- Guieu, C., Bonnet, S., Wagener, T., Loÿe-Pilot, M.D., 2005. Biomass burning as a source of dissolved iron to the open ocean? Geophys. Res. Lett. 32, 1–5.
- Hamilton, D.S., Perron, M.M.G., Bond, T.C., Bowie, A.R., Buchholz, R.R., Guieu, C., Ito, A., Maenhaut, W., Myriokefalitakis, S., Olgun, N., Rathod, S.D., Schepanski, K.,

- Tagliabue, A., Wagner, R., Mahowald, N.M., 2022. Earth, wind, fire, and pollution: aerosol nutrient sources and impacts on ocean biogeochemistry. Ann. Rev. Mar. Sci. 14, 1–28.
- Hamme, R.C., Webley, P.W., Crawford, W.R., Whitney, F.A., DeGrandpre, M.D., Emerson, S.R., Eriksen, C.C., Giesbrecht, K.E., Gower, J.F.R., Kavanaugh, M.T., Peña, M.A., Sabine, C.L., Batten, S.D., Coogan, L.A., Grundle, D.S., Lockwood, D., 2010. Volcanic ash fuels anomalous plankton bloom in subarctic northeast Pacific. Geophys. Res. Lett. 37, 1–5.
- Hans Wedepohl, K., 1995. The composition of the continental crust. Geochim. Cosmochim. Acta 59, 1217–1232.
- Homoky, W.B., Severmann, S., Mills, R.A., Statham, P.J., Fones, G.R., 2009. Pore-fluid Fe isotopes reflect the extent of benthic Fe redox recycling: evidence from continental shelf and deep-sea sediments. Geology 37, 751–754.
- Hunt, H.R., Summers, B.A., Sieber, M., Krisch, S., Al-Hashem, A., Hopwood, M., Achterberg, E.P., Conway, T.M., 2022. Distinguishing the influence of sediments, the Congo River, and water-mass mixing on the distribution of iron and its isotopes in the Southeast Atlantic Ocean. Mar. Chem. 247, 104181.
- Ito, A., 2011. Mega fire emissions in Siberia: potential supply of bioavailable iron from forests to the ocean. Biogeosciences 8, 1679–1697.
- Ito, A., Myriokefalitakis, S., Kanakidou, M., Mahowald, N.M., Scanza, R.A., Hamilton, D. S., Baker, A.R., Jickells, T., Sarin, M., Bikkina, S., Gao, Y., Shelley, R.U., Buck, C.S., Landing, W.M., Bowie, A.R., Perron, M.M.G., Guieu, C., Meskhidze, N., Johnson, M. S., Feng, Y., Kok, J.F., Nenes, A., Duce, R.A., 2019. Pyrogenic iron: the missing link to high iron solubility in aerosols. Sci. Adv. 5, eeau7671.
- Ito, A., Wagai, R., 2017. Data descriptor: global distribution of clay-size minerals on land surface for biogeochemical and climatological studies. Sci. Data 4, 1–11.
- Ito, A., Ye, Y., Baldo, C., Shi, Z., 2021. Ocean fertilization by pyrogenic aerosol iron. npj Clim. Atmos. Sci. 4, 30.
- Jickells, T.D., An, Z.S., Andersen, K.K., Baker, A.R., Bergametti, G., Brooks, N., Cao, J.J., Boyd, P.W., Duce, R.A., Hunter, K.A., Kawahata, H., Kubilay, N., LaRoche, J., Liss, P. S., Mahowald, N., Prospero, J.M., Ridgwell, A.J., Tegen, I., Torres, R., 2005. Global iron connections between desert dust, ocean biogeochemistry, and climate. Science 308, 67–71.
- John, S.G., 2012. Optimizing sample and spike concentrations for isotopic analysis by double-spike ICPMS. J. Anal. At. Spectrom 27, 2123–2131.
- John, S.G., Adkins, J., 2012. The vertical distribution of iron stable isotopes in the North Atlantic near Bermuda. Glob. Biogeochem. Cycles 26, 1–10.
- John, S.G., Helgoe, J., Townsend, E., Weber, T., DeVries, T., Tagliabue, A., Moore, K., Lam, P., Marsay, C.M., Till, C., 2018. Biogeochemical cycling of Fe and Fe stable isotopes in the Eastern Tropical South Pacific. Mar. Chem. 201, 66–76.
- Johnson, C.M., Beard, B.L., Beukes, N.J., Klein, C., O'Leary, J.M., 2003. Ancient geochemical cycling in the Earth as inferred from Fe isotope studies of banded iron formations from the Transvaal Craton. Contrib. to Mineral. Petrol. 144, 523–547.
- Johnson, C., Beard, B., Weyer, S., 2020. Iron Geochemistry: An Isotopic Perspective. Johnson, K.S., Gordon, R.M., Coale, K.H., 1997. What controls dissolved iron concentrations in the world ocean? Mar. Chem. 57, 137–161.
- Johnson, W.K., Miller, L.A., Sutherland, N.E., Wong, C.S., 2005. Iron transport by mesoscale Haida eddies in the Gulf of Alaska. Deep Res. Part II Top. Stud. Oceanogr. 52, 933–953.
- Kajino, M., Hagino, H., Fujitani, Y., Morikawa, T., Fukui, T., Onishi, K., Okuda, T., Kajikawa, T., Igarashi, Y., 2020. Modeling transition metals in East Asia and Japan and its emission sources. GeoHealth 4, 1–22.
- Kanayama, S., Yabuki, S., Yanagisawa, F., Motoyama, R., 2002. The chemical and strontium isotope composition of atmospheric aerosols over Japan: the contribution of long-range-transported Asian dust (Kosa). Atmos. Environ. 36, 5159–5175.
- Koffman, B.G., Yoder, M.F., Methven, T., Hanschka, L., 2021. Glacial dust surpasses both volcanic ash and desert dust in its iron fertilization potential. Global Biogeochem. Cycles 35, 1–29.
- Kondo, Y., Bamba, R., Obata, H., Nishioka, J., Takeda, S., 2021. Distinct profiles of size-fractionated iron-binding ligands between the eastern and western subarctic Pacific. Sci. Rep. 11, 2053.
- König, D., Conway, T.M., Hamilton, D.S., Tagliabue, A., 2022. Surface ocean biogeochemistry regulates the impact of anthropogenic aerosol Fe deposition on the cycling of iron and iron isotopes in the North Pacific. Geophys. Res. Lett. 49, 1–10.
- Kurisu, M., Sakata, K., Miyamoto, C., Takaku, Y., Iizuka, T., Takahashi, Y., 2016a. Variation of iron isotope ratios in anthropogenic materials emitted through combustion processes. Chem. Lett. 45, 970–972.
- Kurisu, M., Takahashi, Y., Iizuka, T., Uematsu, M., 2016b. Very low isotope ratio of iron in fine aerosols related to its contribution to the surface ocean. J. Geophys. Res. Atmos. 121, 11119–11136.
- Kurisu, M., Adachi, K., Sakata, K., Takahashi, Y., 2019. Stable isotope ratios of combustion iron produced by evaporation in a steel plant. ACS Earth Sp. Chem. 3, 588–598.
- Kurisu, M., Sakata, K., Uematsu, M., Ito, A., Takahashi, Y., 2021. Contribution of combustion Fe in marine aerosols over the northwestern Pacific estimated by Fe stable isotope ratios. Atmos. Chem. Phys. 21, 16027–16050.
- Labatut, M., Lacan, F., Pradoux, C., Chmeleff, J., Radic, A., Murray, J.W., Poitrasson, F., Johansen, A.M., Thil, F., 2014. Iron sources and dissolved-particulate interactions in the seawater of the Western Equatorial Pacific, iron isotope perspectives. Glob. Biogeochem. Cycles 28, 1044–1065.
- Lam, P.J., Bishop, J.K.B., 2008. The continental margin is a key source of iron to the HNLC North Pacific Ocean. Geophys. Res. Lett. 35, 1–5.
- Li, R., Zhang, H., Wang, F., He, Y., Huang, C., Luo, L., Dong, S., Jia, X., Tang, M., 2022. Mass fractions, solubility, speciation and isotopic compositions of iron in coal and municipal waste fly ash. Sci. Total Environ. 838, 155974.

- Li, R., Dong, S., Huang, C., Yu, F., Wang, F., Li, X., Zhang, H., Ren, Y., Guo, M., Chen, Q., Ge, B., Tang, M., 2023. Evaluating the effects of contact time and leaching solution on measured solubilities of aerosol trace metals. Appl. Geochem. 148, 1–11.
- Li, W., Xu, L., Liu, X., Zhang, J., Lin, Y., Yao, X., Gao, H., Zhang, D., Chen, J., Wang, W., Harrison, R.M., Zhang, X., Shao, L., Fu, P., Nenes, A., Shi, Z., 2017. Air pollution–aerosol interactions produce more bioavailable iron for ocean ecosystems. Sci. Adv. 3. 1–7.
- Lu, W., Zhao, W., Balsam, W., Lu, H., Liu, P., Lu, Z., Ji, J., 2017. Iron mineralogy and speciation in clay-sized fractions of Chinese desert sediments. J. Geophys. Res. Atmos. 122, 13458–13471.
- Mahowald, N.M., Baker, A.R., Bergametti, G., Brooks, N., Duce, R.A., Jickells, T.D., Kubilay, N., Prospero, J.M., Tegen, I., 2005. Atmospheric global dust cycle and iron inputs to the ocean. Glob. Biogeochem. Cycles 19, GB4025.
- Mahowald, N.M., Engelstaedter, S., Luo, C., Sealy, A., Artaxo, P., Benitez-Nelson, C., Bonnet, S., Chen, Y., Chuang, P.Y., Cohen, D.D., Dulac, F., Herut, B., Johansen, A.M., Kubilay, N., Losno, R., Maenhaut, W., Paytan, A., Prospero, J.M., Shank, L.M., Siefert, R.L., 2009. Atmospheric iron deposition: global distribution, variability, and human perturbations. Ann. Rev. Mar. Sci. 1, 245–278.
- Mahowald, N.M., Hamilton, D.S., Mackey, K.R.M., Moore, J.K., Baker, A.R., Scanza, R.A., Zhang, Y., 2018. Aerosol trace metal leaching and impacts on marine microorganisms. Nat. Commun. 9, 2614.
- Majestic, B.J., Anbar, A.D., Herckes, P., 2009. Stable isotopes as a tool to apportion atmospheric iron. Environ. Sci. Technol. 43, 4327–4333.
- Marsay, C.M., Kadko, D., Landing, W.M., Buck, C.S., 2022. Bulk aerosol trace element concentrations and deposition fluxes during the U.S. GEOTRACES GP15 Pacific meridional transect. Glob. Biogeochem. Cycles 36, 1–21.
- Martin, J.H., Fitzwater, S.E., 1988. Iron deficiency limits phytoplankton growth in the north-east Pacific subarctic. Nature 331, 341–343.
- Martin, J.H., Gordon, R.M., Fitzwater, S., Broenkow, W.W., 1989. Vertex: Phytoplankton/iron studies in the Gulf of Alaska. Deep Sea Res Part A. Oceanogr. Res. Pap. 36, 649–680.
- Maters, E.C., Delmelle, P., Bonneville, S., 2016. Atmospheric processing of volcanic glass: effects on iron solubility and redox speciation. Environ. Sci. Technol. 50, 5033–5040.
- Maters, E.C., Mulholland, D.S., Flament, P., de Jong, J., Mattielli, N., Deboudt, K., Dhont, G., Bychkov, E., 2022. Laboratory study of iron isotope fractionation during dissolution of mineral dust and industrial ash in simulated cloud water. Chemosphere 299, 134472.
- McDuffie, E.E., Martin, R.V., Spadaro, J.V., Burnett, R., Smith, S.J., O'Rourke, P., Hammer, M.S., van Donkelaar, A., Bindle, L., Shah, V., Jaeglé, L., Luo, G., Yu, F., Adeniran, J.A., Lin, J., Brauer, M., 2021. Source sector and fuel contributions to ambient PM2.5 and attributable mortality across multiple spatial scales. Nat. Commun. 12, 3594.
- Mead, C., Herckes, P., Majestic, B.J., Anbar, A.D., 2013. Source apportionment of aerosol iron in the marine environment using iron isotope analysis. Geophys. Res. Lett. 40, 5722–5727.
- Measures, C.I., Brown, M.T., Vink, S., 2005. Dust deposition to the surface waters of the western and central North Pacific inferred from surface water dissolved aluminum concentrations. Geochem. Geophys. Geosyst. 6, 1–16.
- Mori, I., Sun, Z., Ukachi, M., Nagano, K., McLeod, C.W., Cox, A.G., Nishikawa, M., 2008. Development and certification of the new NIES CRM 28: urban aerosols for the determination of multielements. Anal. Bioanal. Chem. 391, 1997–2003.
- Morton, P.L., Landing, W.M., Hsu, S.C., Milne, A., Aguilar-Islas, A.M., Baker, A.R.,
  Bowie, A.R., Buck, C.S., Gao, Y., Gichuki, S., Hastings, M.G., Hatta, M., Johansen, A.
  M., Losno, R., Mead, C., Patey, M.D., Swarr, G., Vandermark, A., Zamora, L.M., 2013.
  Methods for the sampling and analysis of marine aerosols: results from the 2008
  GEOTRACES aerosol intercalibration experiment. Limnol. Oceanogr. Methods 11, 62–78
- Mulholland, D.S., Flament, P., de Jong, J., Mattielli, N., Deboudt, K., Dhont, G., Bychkov, E., 2021. In-cloud processing as a possible source of isotopically light iron from anthropogenic aerosols: New insights from a laboratory study. Atmos. Environ. 259, 118505.
- Myriokefalitakis, S., Ito, A., Kanakidou, M., Nenes, A., Krol, M.C., Mahowald, N.M., Scanza, R.A., Hamilton, D.S., Johnson, M.S., Meskhidze, N., Kok, J.F., Guieu, C., Baker, A.R., Jickells, T.D., Sarin, M.M., Bikkina, S., Shelley, R., Bowie, A., Perron, M. M.G., Duce, R.A., 2018. Reviews and syntheses: the GESAMP atmospheric iron deposition model intercomparison study. Biogeosciences 15, 6659–6684.
- Nishikawa, M., Hao, Q., Morita, M., 2000. Preparation and evaluation of certified reference materials for Asian mineral dust. Glob. Environ. Res. 4, 103–113.
- Nishioka, J., Obata, H., 2017. Dissolved iron distribution in the western and central subarctic Pacific: HNLC water formation and biogeochemical processes. Limnol. Oceanogr. 62, 2004–2022.
- Nishioka, J., Takeda, S., Wong, C.S., Johnson, W.K., 2001. Size-fractionated iron concentrations in the northeast Pacific Ocean: distribution of soluble and small colloidal iron. Mar. Chem. 74, 157–179.
- Nishioka, J., Ono, T., Saito, H., Nakatsuka, T., Takeda, S., Yoshimura, T., Suzuki, K., Kuma, K., Nakabayashi, S., Tsumune, D., Mitsudera, H., Johnson, W.K., Tsuda, A., 2007. Iron supply to the western subarctic Pacific: importance of iron export from the Sea of Okhotsk. J. Geophys. Res. 112, C10012.
- Nishioka, J., Ono, T., Saito, H., Sakaoka, K., Yoshimura, T., 2011. Oceanic iron supply mechanisms which support the spring diatom bloom in the Oyashio region, western subarctic Pacific. J. Geophys. Res. Ocean. 116, 1–17.
- Nishioka, J., Nakatsuka, T., Ono, K., Volkov, Y.N., Scherbinin, A., Shiraiwa, T., 2014. Quantitative evaluation of iron transport processes in the Sea of Okhotsk. Prog. Oceanogr. 126, 180–193.

- Nishioka, J., Obata, H., Ogawa, H., Ono, K., Yamashita, Y., Lee, K., Takeda, S., Yasuda, I., 2020. Subpolar marginal seas fuel the North Pacific through the intermediate water at the termination of the global ocean circulation. Proc. Natl. Acad. Sci. 117, 1–9
- Nishioka, J., Obata, H., Hirawake, T., Kondo, Y., Yamashita, Y., Misumi, K., Yasuda, I., 2021. A review: iron and nutrient supply in the subarctic Pacific and its impact on phytoplankton production. J. Oceanogr. 77, 561–587.
- Nomura, M., Koyama, A., 1996. Design and performance of a new XAFS beamline at the Photon Factory; BL-12C. KEK Rep. 95-15 27, 1.
- Nriagu, J.O., Pacyna, J.M., 1988. Quantitative assessment of worldwide contamination of air, water and soils by trace metals. Nature 333, 134–139.
- Parrington, J.R., Zoller, W.H., 1984. Diurnal and longer-term temporal changes in the composition of atmospheric particles at Mauna Loa, Hawaii. J. Geophys. Res. Atmos. 89, 2522–2534.
- Pattammattel, A., Leppert, V.J., Aronstein, P., Robinson, M., Mousavi, A., Sioutas, C., Forman, H.J., O'Day, P.A., 2021. Iron speciation in particulate matter (PM2.5) from urban Los Angeles using spectro-microscopy methods. Atmos. Environ. 245, 117988.
- Perron, M.M.G., Meyerink, S., Corkill, M., Strzelec, M., Proemse, B.C., Gault-Ringold, M., Sanz, R.E., Chase, Z., Bowie, A.R., 2022. Trace elements and nutrients in wildfire plumes to the southeast of Australia. Atmos. Res. 270, 106084.
- Pinedo-González, P., Hawco, N.J., Bundy, R.M., Armbrust, E.V., Follows, M.J., Cael, B.B., White, A.E., Ferrón, S., Karl, D.M., John, S.G., 2020. Anthropogenic Asian aerosols provide Fe to the North Pacific Ocean. Proc. Natl. Acad. Sci. 117, 27862–27868.
- Radic, A., Lacan, F., Murray, J.W., 2011. Iron isotopes in the seawater of the equatorial Pacific Ocean: new constraints for the oceanic iron cycle. Earth Planet. Sci. Lett. 306, 1–10
- Reid, J.L., 1965. Intermediate Waters of the Pacific Ocean, 2nd ed. The Johns Hopkins University Press, Baltimore.
- Revels, B.N., Zhang, R., Adkins, J.F., John, S.G., 2015. Fractionation of iron isotopes during leaching of natural particles by acidic and circumneutral leaches and development of an optimal leach for marine particulate iron isotopes. Geochim. Cosmochim. Acta 166, 92–104.
- Rudge, J.F., Reynolds, B.C., Bourdon, B., 2009. The double spike toolbox. Chem. Geol. 265, 420–431.
- Rudnick, R.L., Gao, S., 2014. Composition of the continental crust. In: Treatise on Geochemistry. Elsevier, pp. 1-51.
- Sakata, K., Kurisu, M., Tanimoto, H., Sakaguchi, A., Uematsu, M., Miyamoto, C., Takahashi, Y., 2018. Custom-made PTFE filters for ultra-clean size-fractionated aerosol sampling for trace metals. Mar. Chem. 206, 100–108.
- Sakata, K., Kurisu, M., Takeichi, Y., Sakaguchi, A., Tanimoto, H., Tamenori, Y., Matsuki, A., Takahashi, Y., 2022. Iron (Fe) speciation in size-fractionated aerosol particles in the Pacific Ocean: the role of organic complexation of Fe with humic-like substances in controlling Fe solubility. Atmos. Chem. Phys. 22, 9461–9482.
- Sakata, K., Sakaguchi, A., Yamakawa, Y., Miyamoto, C., Kurisu, M., Takahashi, Y., 2023. Measurement report: Stoichiometry of dissolved iron and aluminum as an indicator of the factors controlling the fractional solubility of aerosol iron – results of the annual observations of size-fractionated aerosol particles in Japan. Atmos. Chem. Phys. 23, 9815–9836.
- Schallenberg, C., Davidson, A.B., Simpson, K.G., Miller, L.A., Cullen, J.T., 2015. Iron(II) variability in the northeast subarctic Pacific Ocean. Mar. Chem. 177, 33–44.

### Schlitzer, R., 2020. Ocean Data View.

- Schoenberg, R., Von Blanckenburg, F., 2005. An assessment of the accuracy of stable Fe isotope ratio measurements on samples with organic and inorganic matrices by high-resolution multicollector ICP-MS. Int. J. Mass Spectrom. 242, 257–272.
- Schroth, A.W., Crusius, J., Sholkovitz, E.R., Bostick, B.C., 2009. Iron solubility driven by speciation in dust sources to the ocean. Nat. Geosci. 2, 337–340.
- Schroth, A.W., Crusius, J., Chever, F., Bostick, B.C., Rouxel, O.J., 2011. Glacial influence on the geochemistry of riverine iron fluxes to the Gulf of Alaska and effects of deglaciation. Geophys. Res. Lett. 38, L16605.
- Schroth, A.W., Crusius, J., Gassó, S., Moy, C.M., Buck, N.J., Resing, J.A., Campbell, R.W., 2017. Atmospheric deposition of glacial iron in the Gulf of Alaska impacted by the position of the Aleutian Low. Geophys. Res. Lett. 44, 5053–5061.
- Sedwick, P.N., Sholkovitz, E.R., Church, T.M., 2007. Impact of anthropogenic combustion emissions on the fractional solubility of aerosol iron: Evidence from the Sargasso Sea. Geochem. Geophys. Geosyst. 8, 1–41.
- Seinfeld, J.H., Pandis, S.N., 2006. Atmospheric Chemistry and Physics: From Air Pollution to Climate Change, second edition. John Wiley & Sons Inc., New York.
- Severmann, S., McManus, J., Berelson, W.M., Hammond, D.E., 2010. The continental shelf benthic iron flux and its isotope composition. Geochim. Cosmochim. Acta 74, 3984–4004.
- Sieber, M., Conway, T.M., de Souza, G.F., Hassler, C.S., Ellwood, M.J., Vance, D., 2021. Isotopic fingerprinting of biogeochemical processes and iron sources in the iron-limited surface Southern Ocean. Earth Planet. Sci. Lett. 567, 116967.
- Siebert, C., Nägler, T.F., Kramers, J.D., 2001. Determination of molybdenum isotope fractionation by double-spike multicollector inductively coupled plasma mass spectrometry. Geochem. Geophys. Geosyst. 2, 1–16.
- Sohrin, Y., Urushihara, S., Nakatsuka, S., Kono, T., Higo, E., Minami, T., Norisuye, K., Umetani, S., 2008. Multielemental determination of GEOTRACES key trace metals in seawater by ICPMS after preconcentration using an ethylenediaminetriacetic acid chelating resin. Anal. Chem. 80, 6267–6273.
- Stein, A.F., Draxler, R.R., Rolph, G.D., Stunder, B.J.B., Cohen, M.D., Ngan, F., 2015. Noaa's hysplit atmospheric transport and dispersion modeling system. Bull. Am. Meteorol. Soc. 96, 2059–2077.
- Tagliabue, A., Sallée, J.B., Bowie, A.R., Lévy, M., Swart, S., Boyd, P.W., 2014. Surface-water iron supplies in the Southern Ocean sustained by deep winter mixing. Nat. Geosci. 7, 314–320.

- Takahashi, Y., Higashi, M., Furukawa, T., Mitsunobu, S., 2011. Change of iron species and iron solubility in Asian dust during the long-range transport from western China to Japan. Atmos. Chem. Phys. 11, 11237–11252.
- Takahashi, Y., Furukawa, T., Kanai, Y., Uematsu, M., Zheng, G., Marcus, M.A., 2013.
  Seasonal changes in Fe species and soluble Fe concentration in the atmosphere in the Northwest Pacific region based on the analysis of aerosols collected in Tsukuba, Japan. Atmos. Chem. Phys. 13, 7695–7710.
- Takahashi, T., Sutherland, S.C., Sweeney, C., Poisson, A., Metzl, N., Tilbrook, B., Bates, N., Wanninkhof, R., Feely, R.A., Sabine, C., Olafsson, J., Nojiri, Y., 2002. Global sea-air CO2 flux based on climatological surface ocean pCO2, and seasonal biological and temperature effects. Deep Sea Res Part II: Top. Stud. Oceanogr. 49, 1601–1622
- Taylor, S.R., 1964. Abundance of chemical elements in the continental crust: a new table. Geochim. Cosmochim. Acta 28, 1273–1285.
- Taylor, S.R., McLennan, S.M., 1995. The geochemical evolution of the continental crust. Rev. Geophys. 33, 241–265.
- Tian, H., van Manen, M., Bunnell, Z.B., Jung, J., Lee, S.H., Kim, T.-W., Reichart, G., Conway, T.M., Middag, R., 2023. Biogeochemistry of iron in coastal Antarctica: isotopic insights for external sources and biological uptake in the Amundsen Sea polynyas. Geochim. Cosmochim. Acta 363, 51–67.
- Tsuda, A., Takeda, S., Saito, H., Nishioka, J., Nojiri, Y., Kudo, I., Kiyosawa, H., Shiomoto, A., Imai, K., Ono, T., Shimamoto, A., Tsumune, D., Yoshimura, T., Aono, T., Hinuma, A., Kinugasa, M., Suzuki, K., Sohrin, Y., Noiri, Y., Tani, H., Deguchi, Y., Tsurushima, N., Ogawa, H., Fukami, K., Kuma, K., Saino, T., 2003. A mesoscale iron enrichment in the Western subarctic Pacific induces a large centric diatom bloom. Science 300, 958–961.
- Tsuda, A., Takeda, S., Saito, H., Nishioka, J., Kudo, I., Nojiri, Y., Suzuki, K., Uematsu, M., Wells, M.L., Tsumune, D., Yoshimura, T., Aono, T., Aramaki, T., Cochlan, W.P., Hayakawa, M., Imai, K., Isada, T., Iwamoto, Y., Johnson, W.K., Kameyama, S., Kato, S., Kiyosawa, H., Kondo, Y., Levasseur, M., Machida, R.J., Nagao, I., Nakagawa, F., Nakanishi, T., Nakatsuka, S., Narita, A., Noiri, Y., Obata, H., Ogawa, H., Oguma, K., Ono, T., Sakuragi, T., Sasakawa, M., Sato, M., Shimamoto, A., Takata, H., Trick, C.G., Watanabe, Y.W., Wong, C.S., Yoshie, N., 2007. Evidence for the grazing hypothesis: grazing reduces phytoplankton responses of the HNLC ecosystem to iron enrichment in the western subarctic pacific (SEEDS II).

  J. Oceanogr. 63, 983–994.
- Turekian, K.K., Wedepohl, K.H., 1961. Distribution of the elements in some major units of the Earth's crust. Geol. Soc. Am. Bull. 72, 175–192.

- Uchimoto, K., Nakamura, T., Nishioka, J., Mitsudera, H., Misumi, K., Tsumune, D., Wakatsuchi, M., 2014. Simulation of high concentration of iron in dense shelf water in the Okhotsk Sea. Prog. Oceanogr. 126, 194–210.
- Uematsu, M., Duce, R.A., Prospero, J.M., Chen, L., Merrill, J.T., McDonald, R.L., 1983. Transport of mineral aerosol from Asia over the North Pacific ocean. J. Geophys. Res. 88, 5343–5352.
- Uematsu, M., Duce, R.A., Prospero, J.M., 1985. Deposition of atmospheric mineral particles in the North Pacific Ocean. J. Atmos. Chem. 3, 123–138.
- Uematsu, M., Toratani, M., Kajino, M., Narita, Y., Senga, Y., Kimoto, T., 2004. Enhancement of primary productivity in the western North Pacific caused by the eruption of the Miyake-jima Volcano. Geophys. Res. Lett. 31, 1–4.
- Var, F., Narita, Y., Tanaka, S., 2000. The concentration, trend and seasonal variation of metals in the atmosphere in 16 Japanese cities shown by the results of National Air Surveillance Network (NASN) from 1974 to 1996. Atmos. Environ. 34, 2755–2770.
- Wang, Y., Wu, L., Hu, W., Li, W., Shi, Z., Harrison, R.M., Fu, P., 2022. Stable iron isotopic composition of atmospheric aerosols: an overview. npj Clim. Atmos. Sci. 5, 1–13.
- Willeke, K., Whitby, K.T., 1975. Atmospheric aerosols: size distribution interpretation. J. Air Pollut. Control Assoc. 25, 529–534.
- Wong, K.H., Nishioka, J., Kim, T., Obata, H., 2022. Long-range lateral transport of dissolved manganese and iron in the subarctic Pacific. J. Geophys. Res. Ocean. 127, 1–16.
- Wu, Y.S., Fang, G.C., Lee, W.J., Lee, J.F., Chang, C.C., Lee, C.Z., 2007b. A review of atmospheric fine particulate matter and its associated trace metal pollutants in Asian countries during the period 1995–2005. J. Hazard. Mater. 143, 511–515.
- Wu, J., Rember, R., Cahill, C., 2007a. Dissolution of aerosol iron in the surface waters of the North Pacific and North Atlantic oceans as determined by a semicontinuous flowthrough reactor method. Glob. Biogeochem. Cycles 21, 1–10.
- Xiu, P., Palacz, A.P., Chai, F., Roy, E.G., Wells, M.L., 2011. Iron flux induced by Haida eddies in the Gulf of Alaska. Geophys. Res. Lett. 38, 1–5.
- Yasuda, I., Hiroe, Y., Komatsu, K., Kawasaki, K., Joyce, T.M., Bahr, F., Kawasaki, Y., 2001. Hydrographic structure and transport of the Oyashio south of Hokkaido and the formation of North Pacific Intermediate Water. J. Geophys. Res. Ocean. 106, 6931–6942.
- Zhu, Y., Li, W., Lin, Q., Yuan, Q., Liu, L., Zhang, J., Zhang, Y., Shao, L., Niu, H., Yang, S., Shi, Z., 2020b. Iron solubility in fine particles associated with secondary acidic aerosols in east China. Environ. Pollut. 264, 114769.
- Zhu, C., Tian, H., Hao, J., 2020a. Global anthropogenic atmospheric emission inventory of twelve typical hazardous trace elements, 1995–2012. Atmos. Environ. 220, 117061.